Electronic Supplementary Material (ESI) for Journal of Materials Chemistry A.
This journal is © The Royal Society of Chemistry 2018

Supporting Information

Cobalt (oxy)hydroxide nanosheet arrays with exceptional porosity and rich defects as highly efficient oxygen evolution electrocatalyst under neutral condition

Minqi Chen, Yanyu Xie, Jun-Xi Wu, Huanfeng Huang, Jun Teng, Dawei Wang,* Yanan Fan, Ji-Jun Jiang, Hai-Ping Wang, and Cheng-Yong Su*

Section S1. Materials

All chemicals were commercially available and used as obtained without further purification. Cobalt(II) nitrate hexahydrate ($Co(NO_3)_2 \cdot 6H_2O$, Aladdin, Shanghai, A. R.), 2-methylimidazole (2-mIM, Aladdin, A. R.), sodium hypochlorite aqueous solution (NaClO, Damao, Tianjin, 8 wt.% available Cl), ruthenium (IV) oxide powder (RuO_2, Aladdin, >99.0%), iridium (IV) oxide powder (IrO2, Aladdin, >99.0%) and Nafion® D-520 dispersion (Alfa Aesar, 5% w/w in water and 1-propanol). Millipore deionized water (18.2 MΩ·cm) was used to prepare all the solutions. Carbon cloth (WOS 1002) was obtained from CeTech, Taiwan.

Section S2. Synthesis

Synthesis of Co-ZIF-L nanosheet arrays (NSAs) on carbon cloth (denoted as Co-ZIF-L/CC). 2-mIM (0.165 g) and $Co(NO_3)_2 \cdot 6H_2O$ (0.116 g) were mixed in aqueous solution (10 mL) at room temperature. A piece of CC (0.5×2 cm^2) repeatedly rinsed in ultrasonic cleaner with acetone, Milli-Q water and absolute ethanol was then vertically immersed in the solution with an effective contact area of 0.5×1.2 cm^2. After static reaction for 60 minute at room temperature, purple Co-ZIF-L deposits were obtained on the immersed CC. The Co-ZIF-L/CC was taken out of the solution, rinsed with copious Milli-Q water and ethanol, and dried under ambient condition. The mass loading of Co-ZIF-L on CC was measured to be 1.3 mg cm^{-2} by differential weighting method. Co-ZIF-L powder was prepared by following the same synthetic procedure except that (1) the carbon cloth was not used and (2) the powder was collected by centrifugation, washed with water three times, and finally dried at 60 °C overnight.

Synthesis of Cobalt (Oxy)hydroxides on CC (CoO_xH_y/CC). Briefly, an aqueous alkaline solution containing NaClO (4 wt.% available Cl) and KOH (1 M) was freshly prepared and used at room temperature. A piece of Co-ZIF-L/CC (0.5 ×2 cm^2) was immersed in the NaClO aqueous solution

(1.5 mL) and kept at room temperature for 10 min. The Co-ZIF-L/CC after reaction were taken out directly from the solution, carefully rinsed by copious Milli-Q water and ethanol, dried at 60 °C and collected as the final product, CoO_xH_y/CC. The mass loading of CoO_xH_y on CC was measured to be 0.8 mg cm^{-2}.

A series of control samples were also synthesized. The samples synthesized by immersing Co-ZIF-L/CC in solution containing NaClO were denoted as Co-ZIF-L-*x*, in which *x* indicates the reaction time in minute. Accordingly, our target product CoO_xH_y/CC synthesized in NaClO solution after a reaction time of 10 min can also be denoted as Co-ZIF-L-10. Control samples synthesized without NaClO were denoted as Co-ZIF-L-NO-*x*.

Synthesis of CoO_xH_y-NO Nanoplates on CC (CoO_xH_y-NO/CC). A piece of Co-ZIF-L/CC (0.5×2 cm^2) was immersed in KOH aqueous solution (1 M) at room temperature for 120 min, during which the color of Co-ZIF-L/CC changed from light purple to brown. The obtained product was taken out of the solution, rinsed with Milli-Q water and ethanol, and then dried at 60 °C. Following the same immersing procedure but without using CC as the substrate, CoO_xH_y-NO powder was also synthesized and collected.

Section S3. Characterization

The morphologies of all samples were imaged by field emission scanning electron microscopy (FESEM, Hitachi, SU8010) operated at an electron acceleration energy of 1 kV and 10 μA. Transmission electron microscopy (TEM) images and selected-area electron diffraction (SAED) patterns were recorded on a FEI Technai G2 TEM operated at 120 kV. High-resolution TEM

(HRTEM) images, high angle annular dark field scanning transmission electron microscopy (HAADF STEM) images, and energy dispersive X-ray spectrometry (EDX) elemental maps were obtained with JEOL JEM-ARM200F TEM operated at 200 kV. Powder X-ray diffraction (PXRD) patterns were collected on a Rigaku MiniFlex 600 X-ray diffractometer (Cu Kα). X-ray photoelectron spectroscopy (XPS) analyses were carried out on an ESCA Lab250 X-ray photoelectron spectrometer. All XPS spectra were corrected by calibrating C 1s peak at 284.8 eV and data fitting were fitted using XPS peak 4.1 software. Raman spectra were recorded on a Renishaw Micro-Raman Spectrometer using a 10 mW air-cooled aron ion laser (514.5 nm) as the excitation source. Attenuated Total Reflectance Fourier Transform Infrared (ATR-FTIR) spectra were recorded on a Nicolet6700-Contiuμm spectrometer (ThermoFisher Scientific). Electron paramagnetic resonance (EPR) spectra were collected on an EPR spectrometer (A300-10-12, Bruker) in the X-band (9.45 GHz) with 5.00-G modulation amplitude and a magnetic field modulation of 100 kHz at 25 °C. The pH of the electrolytes was measured by a calibrated Mettler Toledo S220 pH meter at 25 °C.

Section S4. Electrochemical Characterization

All electrochemical measurements were performed in a one-compartment glass cell using a Metrohm Autolab electrochemical workstation with the conventional three-electrode configuration. The as-synthesized CoO_xH_y/CC integrated electrodes were partially sealed with Teflon tape (leaving an effective area of 1 cm^2 (0.5 cm × 1 cm × 2 sides)) and directly used as the working electrode for electrochemical characterization. A platinum wire was used as the counter electrode and Hg/HgO as the reference electrode in KOH solution (1 M). The current density was normalized to the geometrical surface area and the measured potential vs. Hg/HgO were converted to a reversible hydrogen electrode (RHE) scale based on the Nernst equation ($E_{RHE} = E_{Hg/HgO} + 0.059 \times pH + 0.098$). In order to ensure the O_2/H_2O equilibrium at 1.23 V *vs.* RHE, the electrochemical

catalytic activity towards oxygen evolution reaction was measured using linear sweep voltammetry (LSV) in the O_2 saturated electrolyte, which was either 1.0 M KOH (pH = 13.7), 0.1 M potassium phosphate buffer (PBS, pH = 7.0) or 1 M PBS (pH = 7.0). LSV curves were recorded at a scan rate of 2 mV s^{-1} under magnetic stirring until the stabilization of the working electrodes by repeated LSV scanning and corrected for the uncompensated resistance (R_u) contribution within the cell at the level of 90%. The R_u for each sample was measured by electrochemical impedance spectroscopy (EIS). The EIS measurements were performed by applying an alternating current (AC) impedance with 10 mV amplitude in a frequency ranging from 10^5 to 0.01 Hz and recorded at 1.55 and 1.61V *vs.* RHE in 1 M KOH solution and 0.1 M PBS, respectively. The cyclic voltammogram was recorded with a scan rate of 5 mV s^{-1} to track Co redox features and the applied potential was corrected for Ohmic losses and referred to RHE under working potential window from open-circuit potential (OCP) to 1.65 V vs. RHE in 0.1 M PBS and 1.60 V vs. RHE in 1 M KOH, respectively. Long-term stability measurements were carried out chronopotentially at a constant current density of 10 mA cm^{-2} (normalized to the electrode geometric area) in either 0.1 M PBS or 1.0 M KOH for 24 h with medium stirring to minimize the accumulation of gas bubbles on the electrode surface.

The Tafel slope was calculated according to the Tafel equation, $\eta/\mathrm{V} = b\log(j/\mathrm{mA}) + a$, where η is the overpotential calculated by $\eta/\mathrm{V} = E$ (vs. RHE) – 1.23, b is the Tafel slope, j is the current density and a is relative to the exchange current density. Acknowledgedly, the overpotential at 10 mA cm^{-2}, the reference current density expected in a previously reported 12.3% efficient solar-to-fuels conversion device, is considered as the benchmark of the electrocatalytic activity for OER or HER.[S1] The electrical double layer specific capacitor (C_{dl}) of the materials were measured from the double–layer charging curves using the CVs within a small potential range of 1.205-1.305 V *vs.* RHE in 1 M KOH solution. The plot of current density ($(j_a-j_c)/2$ at 1.25 V *vs.* RHE) against scan rate has a linear relationship and its slope is the C_{dl}. The electrochemically active surface area (ECSA) of the electrode materials was calculated by ECSA = C_{dl}/C_s, in which C_s, with a typical

value of 40 μF cm^{-2}, is the specific capacitance of a flat, smooth surface of the electrode materials.[S2, 3]

For comparison, commercial catalysts (RuO_2) were immobilized on carbon cloth with Nafion. Briefly, catalyst powder (5 mg), 5% Nafion (50 μL) and water/ethanol (1:1 v/v, 450 μL) were dispersed under ultrasonication for 30 min to form a homogeneous ink and then a specific volume of the ink was pipetted onto the pre-cleaned carbon cloth with a loading equivalent to 1 mg cm^{-2}.

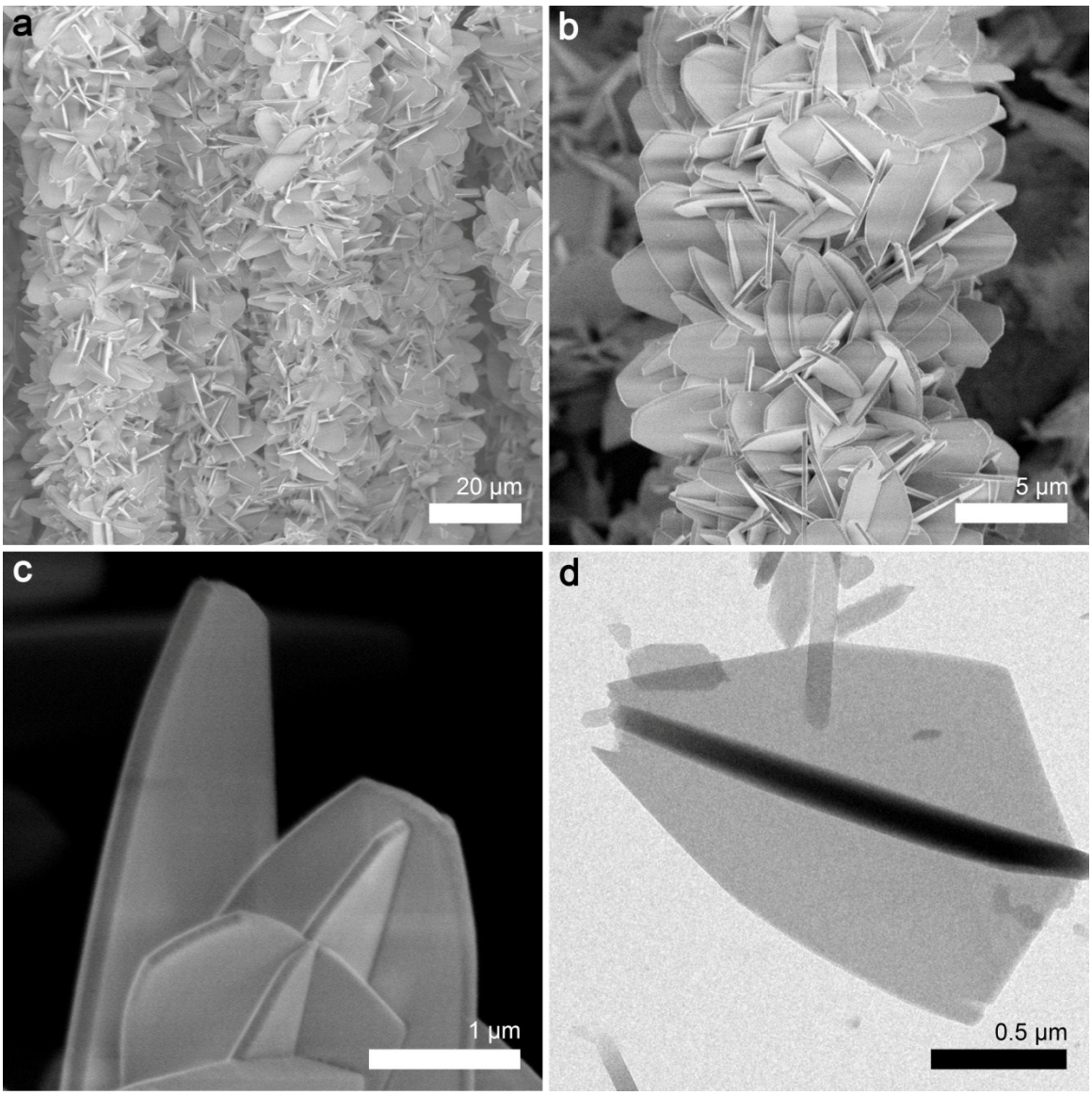

Fig. S1 (a-c) SEM images at different magnification and (d) TEM image of the as-synthesized Co-ZIF-L/CC.

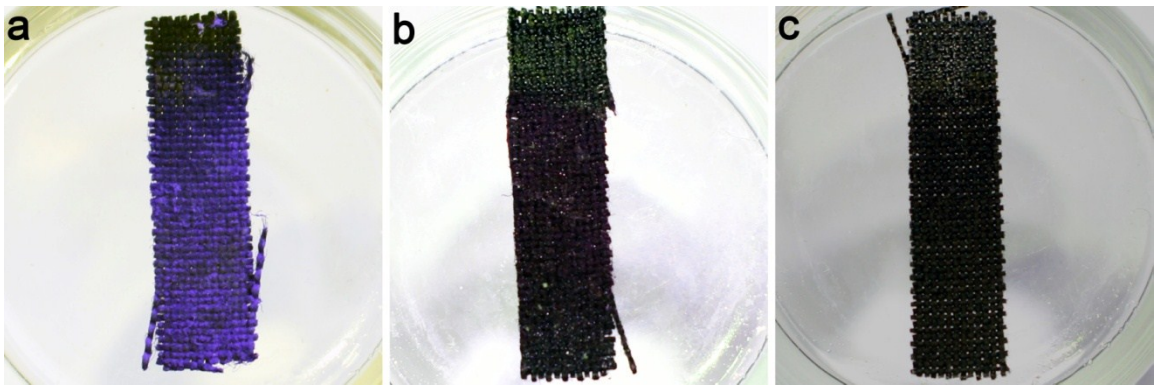

Fig. S2 Optical images of Co-ZIF-L/CC (a) before (purple) and (b-c) after immersing in solution containing KOH (1 M) and NaClO (4 wt.% Cl) for (b) 5 minute (dark purple) and (c) 10 minute (brownish black).

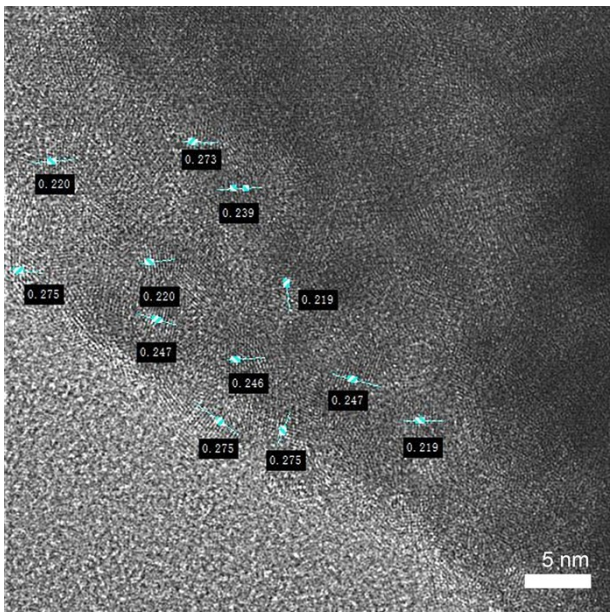

Fig. S3 HRTEM image of CoO_xH_y NS.

To identify the composition of our product by HRTEM, twelve sampling sites are measured, and the corresponding lattice spacing is labeled in Fig. S3 and listed in Table S1 as well. Based on these results, four typical values of the lattice spacing are found, that is, 0.275, 0.239, 0.247, and 0.219 nm. The former two lattice spacing values can be unambiguously assigned to the (100) and (101) planes of β-$Co(OH)_2$ (Table S1 and S2), thus indicating the existence of β-$Co(OH)_2$ in our product. The later two lattice spacing values, however, cannot be easily assigned, as they are close to two sets of data with slight difference, that is, 0.243 nm ((101) plane) and 0.219 nm ((006) plane) of β-$Co(OH)_2$ (PDF #14-0673; Table S2), and 0.246 nm ((111) plane) and 0.213 nm ((200) plane) of CoO (PDF #43-1004 and #48-1719, Table S3). Here, it is worth noting that our product was prepared from Co^{2+}-containing precursor (Co-ZIF-L) at ambient temperature and in the aqueous solution containing concentrated base (1 M KOH) and strong oxidant (NaClO, 4 wt.% available Cl). Such experimental condition is typical for the formation of CoOOH [S4-6] rather than CoO [S7-10]. Moreover, the conversion of $Co(OH)_2$ or CoOOH to CoO is not likely to occur under our experimental condition, as it usually requires temperature much higher than the ambient temperature. Therefore, it would be more reasonable to assign the assign the lattice spacing of 0.247

and 0.219 nm in our product to the (101) and (006) plane of β-$Co(OH)_2$ (PDF #14-0673; Table S1 and S2), respectively.

Furthermore, the ATR-FTIR (Attenuated Total Reflectance Fourier Transform Infrared) spectrum of CoO_xH_y, as an additional and critical experimental evidence for CoOOH, is recorded and shown in Fig. S4. The sharp intra peak centered at 3623 cm^{-1} is assigned to the stretching of dissociative O-H of $Co(OH)_2$, and the broad and strong peak located at 3250-3470 cm^{-1} is due to the existence of abundant associated O-H of CoOOH and some adsorption of water molecules.[S11, 12] The ATR-FTIR spectrum thus further supports the coexistence of $Co(OH)_2$ and CoOOH in CoO_xH_y.

Table S1 Lattice spacing and the corresponding crystalline planes in the HRTEM image of CoO_xH_y NS shown in Fig. S3.

Site No.	Lattice spacing (nm)	Corresponding Compound	Crystalline plane
1	0.220	*β*-CoOOH	(006)
2	0.273	*β*-$Co(OH)_2$	(100)
3	0.239	*β*-$Co(OH)_2$	(101)
4	0.275	*β*-$Co(OH)_2$	(100)
5	0.220	*β*-CoOOH	(006)
6	0.219	*β*-CoOOH	(006)
7	0.247	*β*-CoOOH	(101)
8	0.246	*β*-CoOOH	(101)
9	0.247	*β*-CoOOH	(101)
10	0.275	*β*-$Co(OH)_2$	(100)
11	0.275	*β*-$Co(OH)_2$	(100)
12	0.219	*β*-CoOOH	(006)

Table S2 Structural information retrieved from the standard PDF files of β-$Co(OH)_2$ and β-CoOOH.

Compound	2θ (°)	d (Å)	(hkl)
β-$Co(OH)_2$ PDF #30-0443	19.1	4.6530	(001)
	32.5	**2.7550**	**(100)**
	37.9	**2.3710**	**(101)**
	38.7	2.3270	(002)
	51.4	1.7776	(102)
β-CoOOH PDF #14-0673	20.2	4.3933	(003)
	37.0	**2.4276**	**(101)**
	41.1	**2.194**	**(006)**
	50.7	1.7991	(0150

Table S3 Structural information retrieved from the standard PDF files of CoO, Co_2O_3, and Co_3O_4.

Compound	2θ (°)	d (Å)	(*hkl*)
CoO PDF #43-1004	36.503	2.4595	(111)
	42.401	2.1300	(200)
	61.520	1.5061	(220)
CoO PDF #48-1719	36.492	2.4602	(111)
	42.387	2.1307	(200)
	61.497	1.5066	(220)
CoO PDF #42-1300	34.148	2.6235	(111)
	39.636	2.2720	(200)
	57.301	1.6065	(220）)
Co_2O_3 PDF #02-0770	27.769	3.2100	
	31.137	2.8700	(002)
	38.609	2.3300	(102)
	51.283	1.7800	
Co_3O_4 PDF #43-1003	19.000	4.6670	(111)
	31.271	2.8580	(220)
	36.845	2.4374	(311)
	38.546	2.3337	(222)
	44.808	2.0210	(400)
Co_3O_4 PDF #42-1467	19.000	4.6670	(111)
	31.271	2.8580	(220)
	36.852	2.4370	(311)
	38.541	2.3340	(222)
	44.808	2.0210	(400)

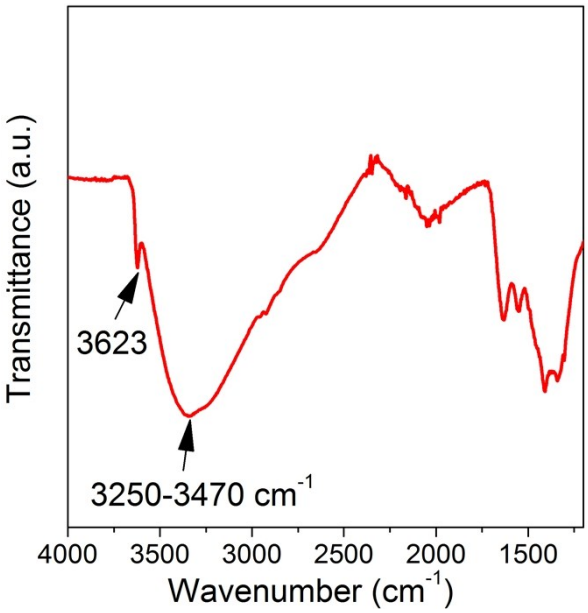

Fig. S4 AT-FTIR spectrum of CoO_xH_y.

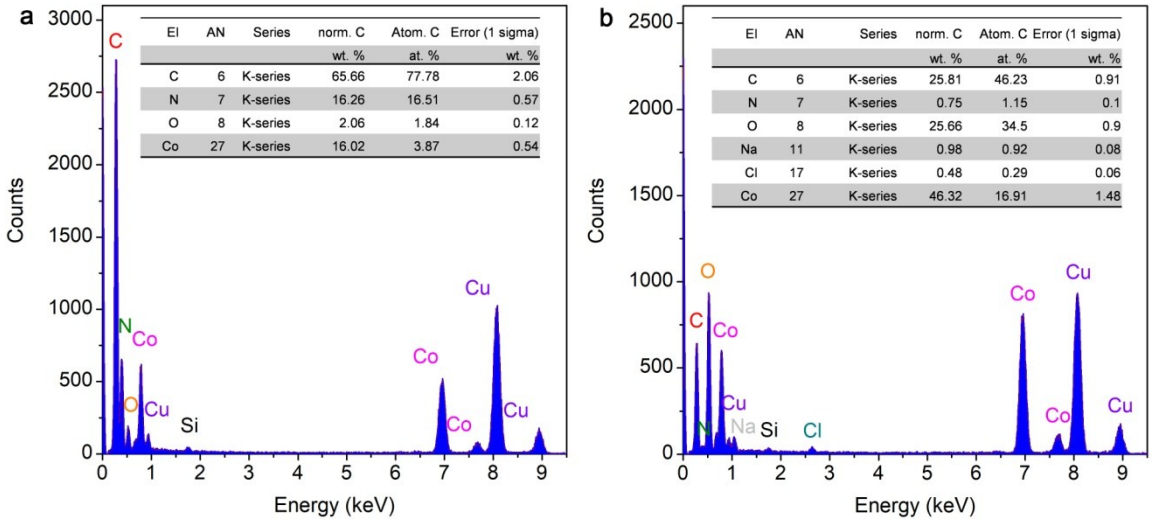

El	AN	Series	norm. C wt. %	Atom. C at. %	Error (1 sigma) wt. %
C	6	K-series	65.66	77.78	2.06
N	7	K-series	16.26	16.51	0.57
O	8	K-series	2.06	1.84	0.12
Co	27	K-series	16.02	3.87	0.54

El	AN	Series	norm. C wt. %	Atom. C at. %	Error (1 sigma) wt. %
C	6	K-series	25.81	46.23	0.91
N	7	K-series	0.75	1.15	0.1
O	8	K-series	25.66	34.5	0.9
Na	11	K-series	0.98	0.92	0.08
Cl	17	K-series	0.48	0.29	0.06
Co	27	K-series	46.32	16.91	1.48

Fig. S5 EDS spectra of (a) Co-ZIF-L/CC and (b) CoO_xH_y/CC.

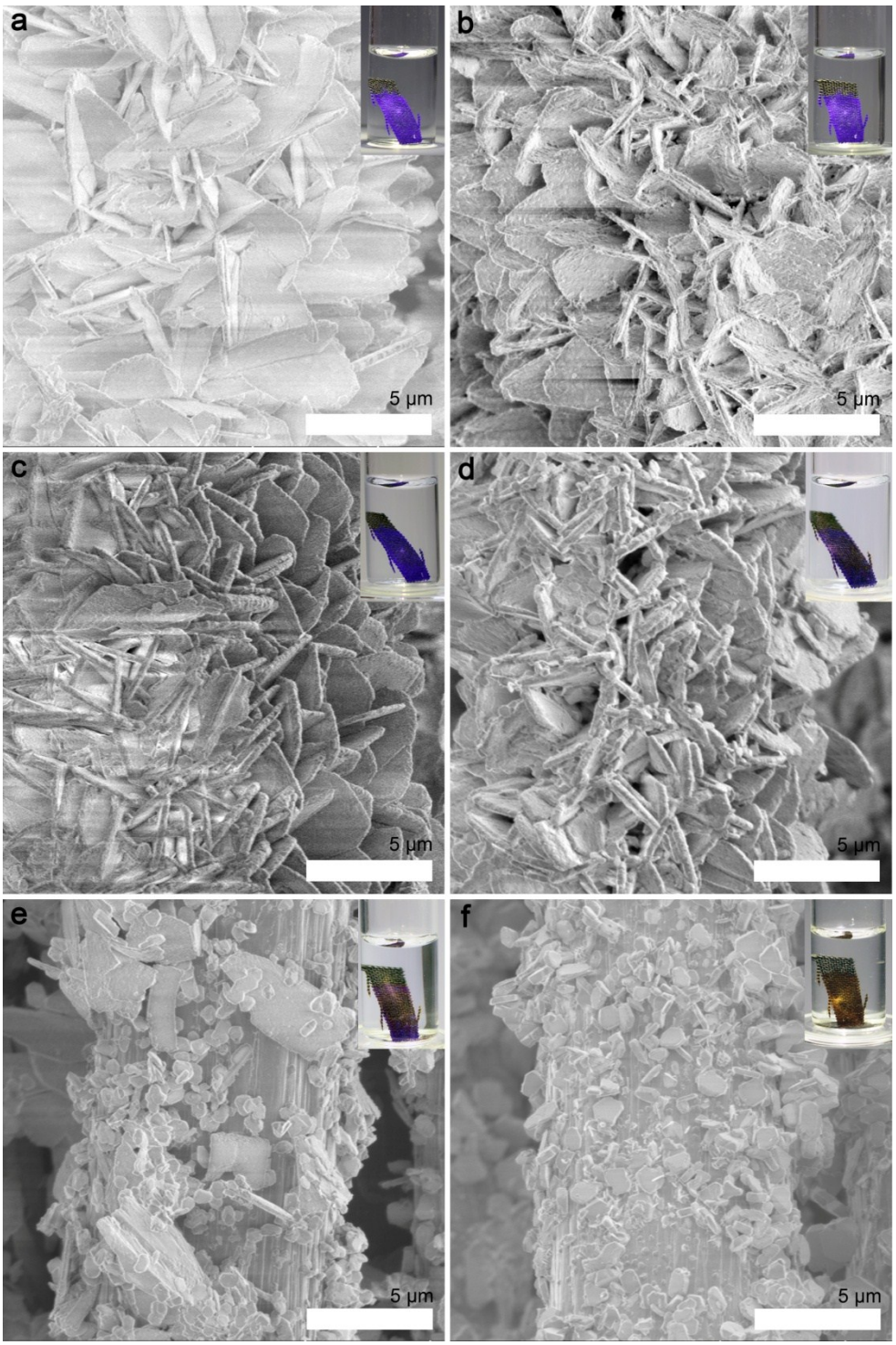

Fig. S6 SEM images and optical images (insets) of Co-ZIF-L/CC after immersing in 1 M KOH solution without NaClO for (a) 5, (b) 10, (c) 30, (d) 60, (e) 90, and (f) 120 minute.

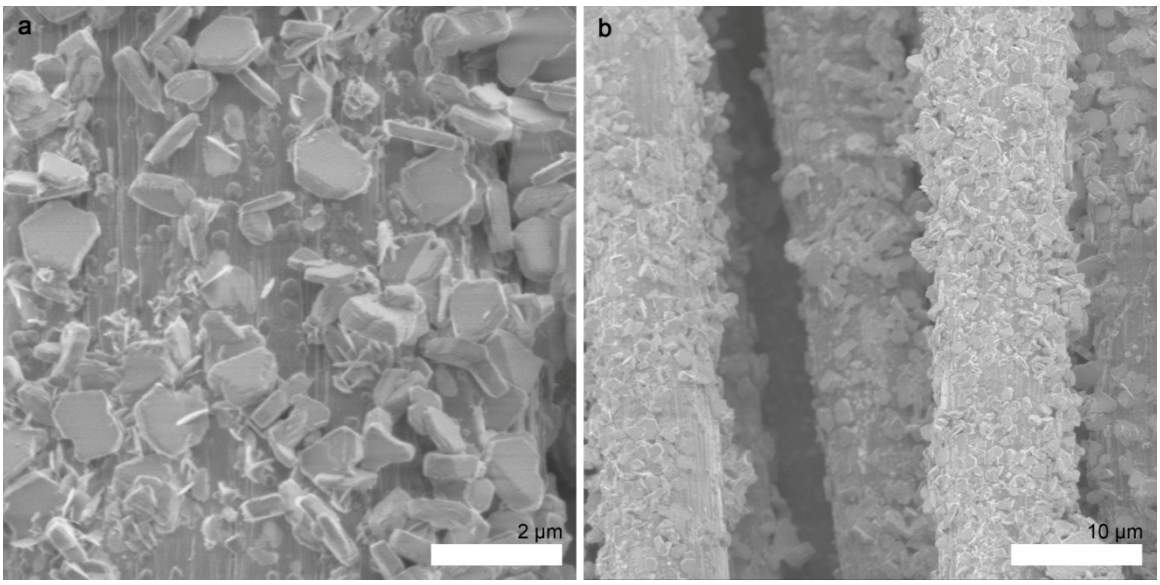

Fig. S7 SEM images of CoO_xH_y-NO/CC at different magnification. The CoO_xH_y-NO/CC were synthesized by immersing Co-ZIF-L/CC in 1 M KOH solution without NaClO for 120 minute.

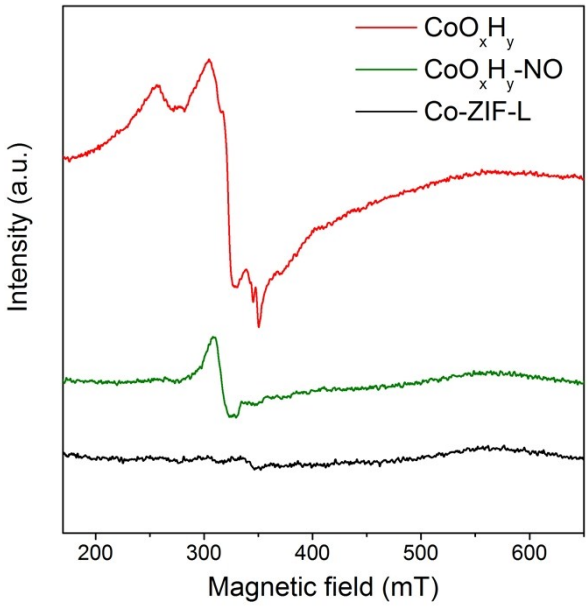

Fig. S8 EPR spectra of CoO_xH_y, CoO_xH_y-NO and Co-ZIF-L.

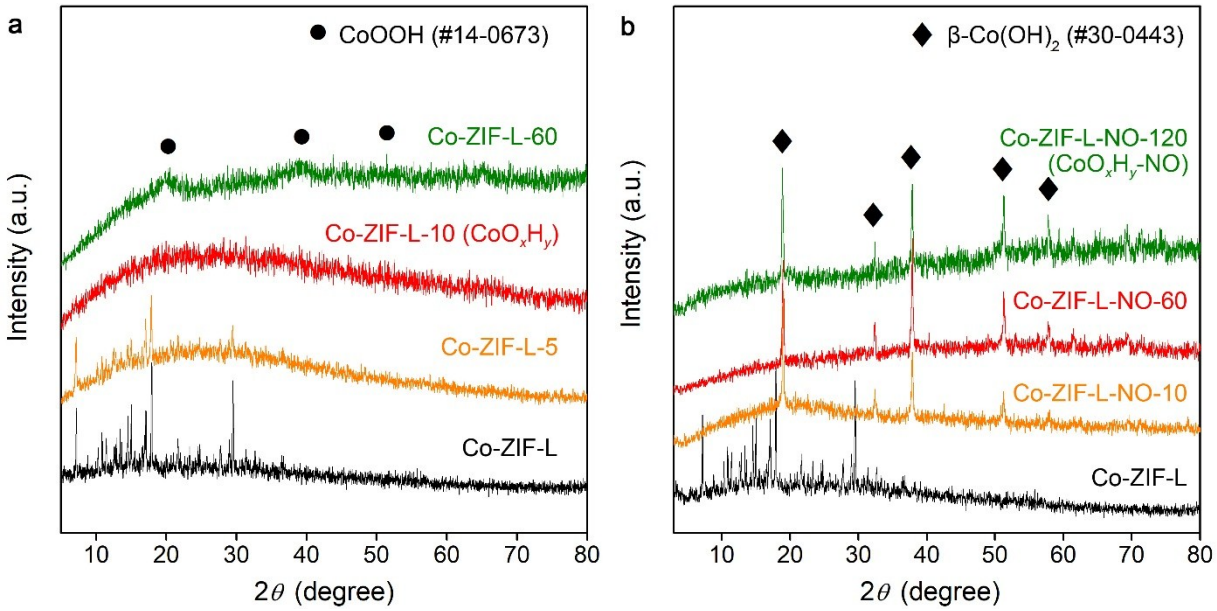

Fig. S9 Time-resolved PXRD patterns of the products synthesized by immersing Co-ZIF-L/CC in 1 M KOH solution (a) with or (b) without NaClO (4 wt.% Cl). The products synthesized with NaClO are denoted as Co-ZIF-L-*x*, where *x* indicates the reaction time (in minute). The products synthesized without NaClO are denoted as Co-ZIF-L-NO-*x*. CoO_xH_y NSAs and CoO_xH_y-NO nanoplates correspond to Co-ZIF-L-10 and Co-ZIF-L-NO-120, respectively.

In addition to the SEM observation (Fig. S1 and Fig. S6-S7), the rapid conversion process of Co-ZIF-L into CoO_xH_y was further investigated by the time-resolved PXRD (Fig. S9), Raman spectroscopy (Fig. S10) and EDS (Fig. S11). In the presence of NaClO, the PXRD and Raman peaks of Co-ZIF-L reduce in 5 minute and completely disappear in 10 minute. Meanwhile, the N/Co atomic ratio tends to stabilize since 10 minute. These results indicate that the conversion of Co-ZIF-L into CoO_xH_y is rapidly completed within 10 minute. The PXRD pattern of the as-prepared CoO_xH_y shows no discernible peaks over the whole 2θ range of 5–80° (Fig. S9a) within the reaction time range of 10-60 minute, indicating a poor crystallinity nature. The appearance of broad peaks assigned to CoOOH start to appear until 60 minute, which is probably due to a gradual self-refinement process of their crystallinity.

By contrast, in the absence of NaClO, although strong peaks assigned to β-$Co(OH)_2$ appear in 10 minute, the Raman peaks corresponding to the Co-ligand of Co-ZIF-L remain after 60 minute and thoroughly disappear until 120 minute (Fig. S11b). Moreover, the N/Co atomic ratio of the products also steadily decreases up to 120 min (Fig. S11a). These results suggest that the complete conversion of Co-ZIF-L into CoO_xH_y-NO can only be achieved after *ca.* 120 min, which is much slower than that with NaClO. Moreover, as indicated by the PXRD patterns collected after 60 minute, the product without NaClO shows better crystallinity than the product with NaClO. Such crystallinity difference should be a consequence of the much slower conversion process without NaClO, which allows a gradual spatial reorganization of Co^{2+} and OH^- into well-crystalized products.

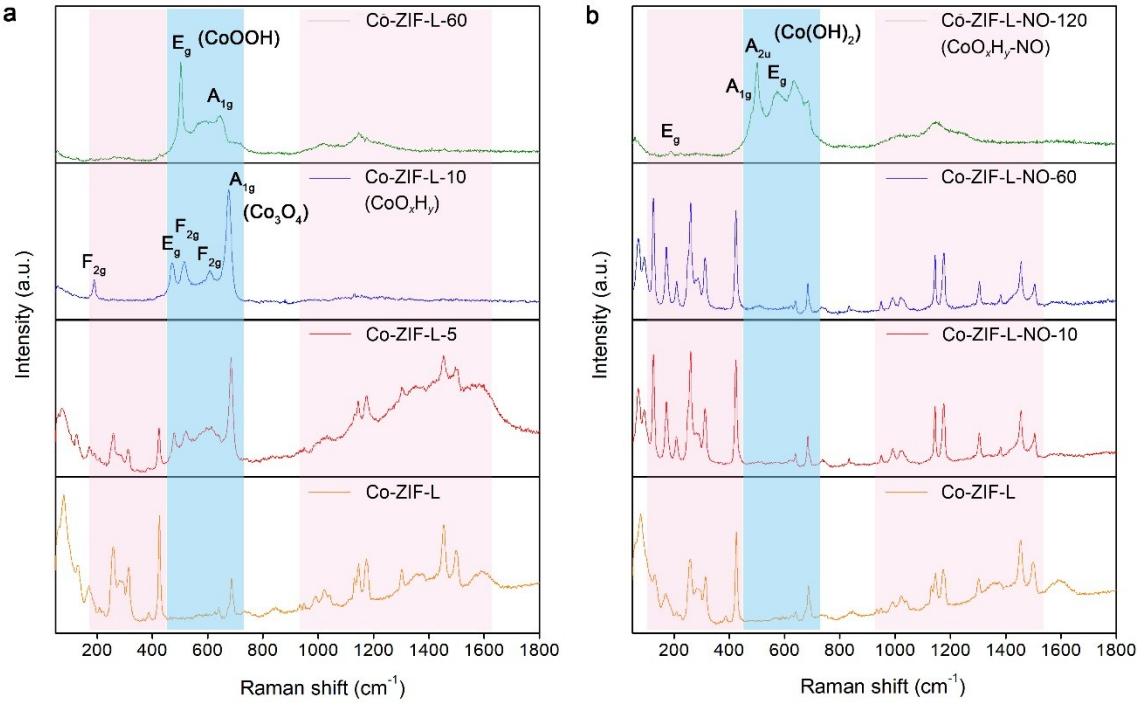

Fig. S10 Time-resolved Raman spectra of products synthesized from Co-ZIF-L (a) with and (b) without NaClO.

With increasing reaction time, the complex multiple vibration peaks of Co-ZIF-L in Raman spectra disappear rapidly (Fig. S10a). After only 10 minute reaction with NaClO, the product shows five typical vibration peaks at 189, 471, 518, 611 and 674 cm^{-1} in the Raman spectrum, which can be assigned to Co_3O_4 that is generated from the vulnerable low-crystalline CoOOH under the laser exposure of Raman test.[S13] Such results confirm the rapid conversion process of Co-ZIF-L in the presence of NaClO. In contrast, the Raman peaks assigned to Co-ligand of Co-ZIF-L (Fig. S10b) remain for 60 minute and thoroughly disappear in 120 minute, confirming a much slower conversion process of Co-ZIF-L without NaClO.

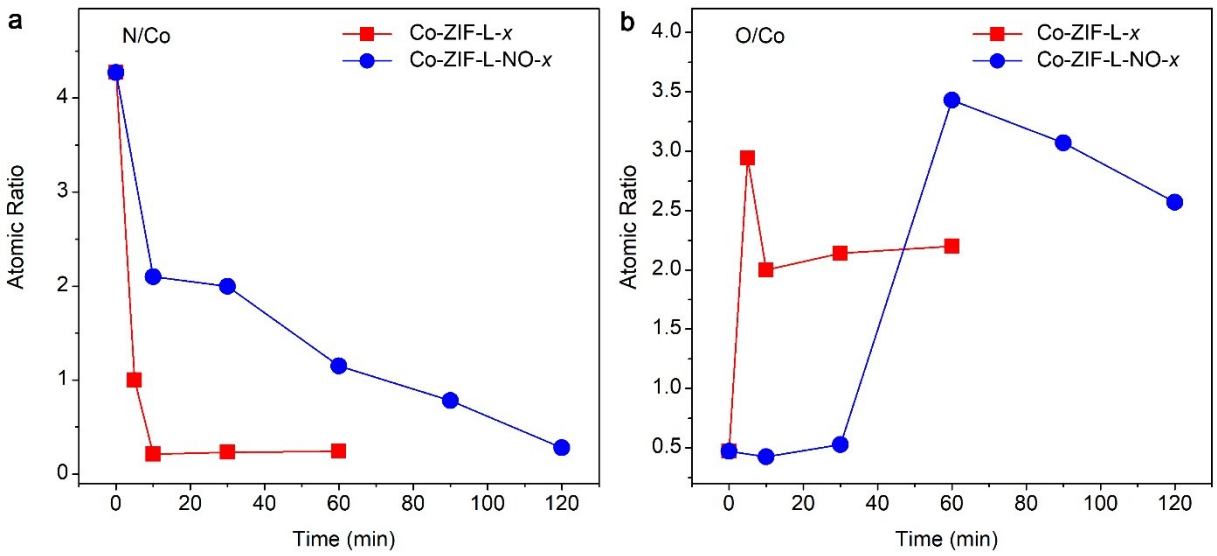

Fig. S11 Time-resolved EDS analysis of the products synthesized from Co-ZIF-L with (red cubes; Co-ZIF-L-*x*) and without (blue circles; Co-ZIF-L-NO-*x*) NaClO. (a) N/Co atomic ratio, (b) O/Co atomic ratio.

The products synthesized with NaClO show a sharp decrease in N/Co ratio from 4.3 (the theoretical value in Co-ZIF-L is 4.0) to as low as 0.2 in 10 minute, and stabilize as reaction time prolongs to 60 minute (Fig. S11a). The presence of negligible N may be attributed by the dissociative N-containing ligand residuals adsorbed in the highly porous products. Meanwhile, the O/Co ratio of the product rapidly increases from *ca*. 0.5 to *ca*. 2.0, the theoretical value of either CoOOH, $Co(OH)_2$ or their mixture. These results confirm that the ligands of precursor were rapidly and adequately exchanged out during the formation of CoO_xH_y in the presence of NaClO. In contrast, without NaClO, the N/Co ratio of ZLCC-OH declines slowly from 4.3 to 0.2 in 120 minute and O/Co ratio increases sharply only after 30 minute, which further verifies the slow conversion process of Co-ZIF-L.

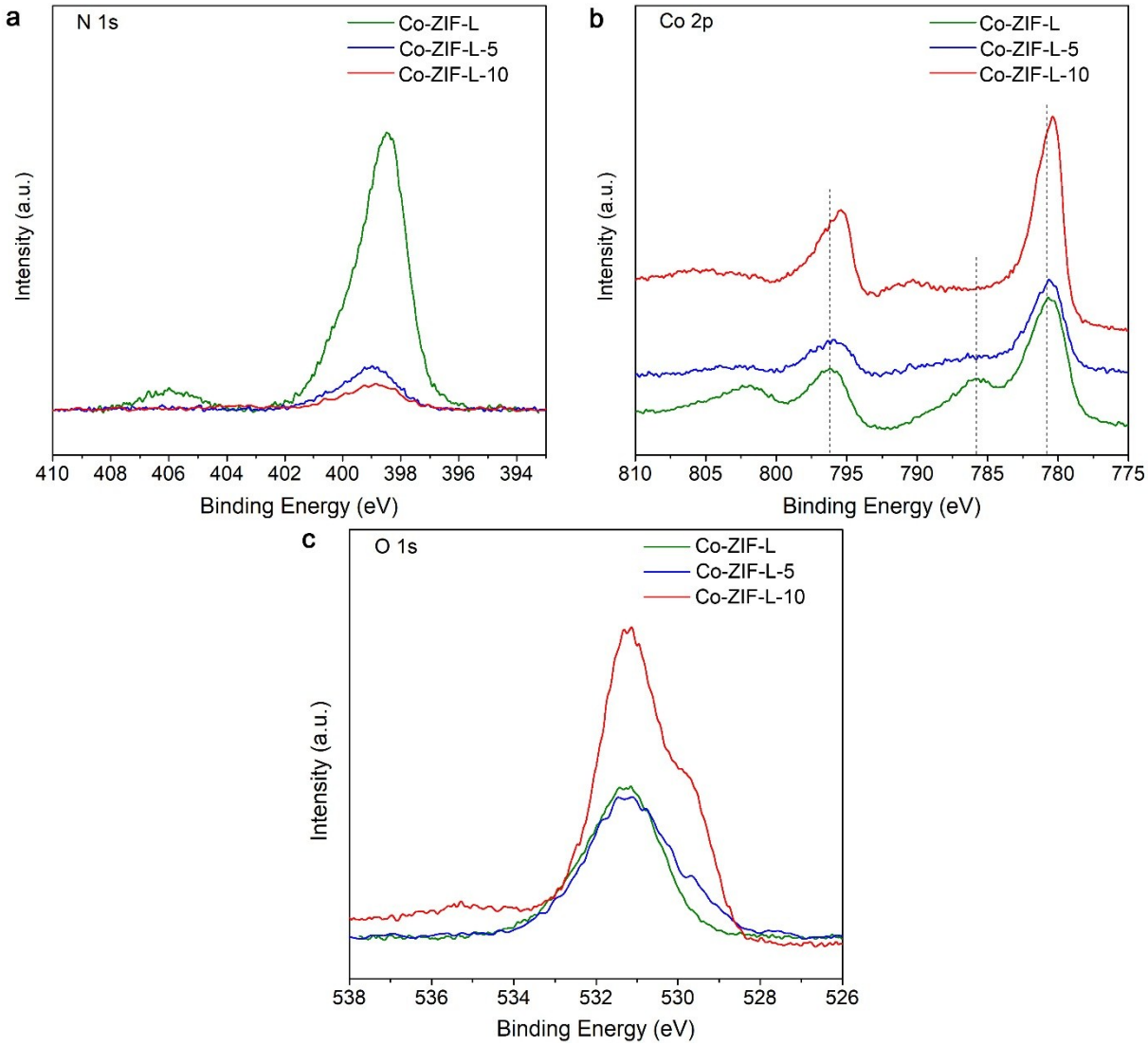

Fig. S12 The changes in (a) Co 2p, (b) O 1s and (c) N 1s peaks in the XPS spectra of the products after treating Co-ZIF-L with NaClO solution for 5 and 10 minute, respectively.

The XPS spectra of N 1s, Co 2p and O 1s in Fig. S12 and Fig. 2a,b confirm the NaClO-induced conversion process of Co-ZIF-L. For instance, as the reaction proceeds, the Co^{2+} in Co-ZIF-L is partially oxidized into Co^{3+}, as indicated by the obvious shifts of the Co $2p_{3/2}$ peak to lower binding energy, the reduced satellite peak at *ca.* 786 eV and the raised satellite peak at *ca.* 790.2 eV.

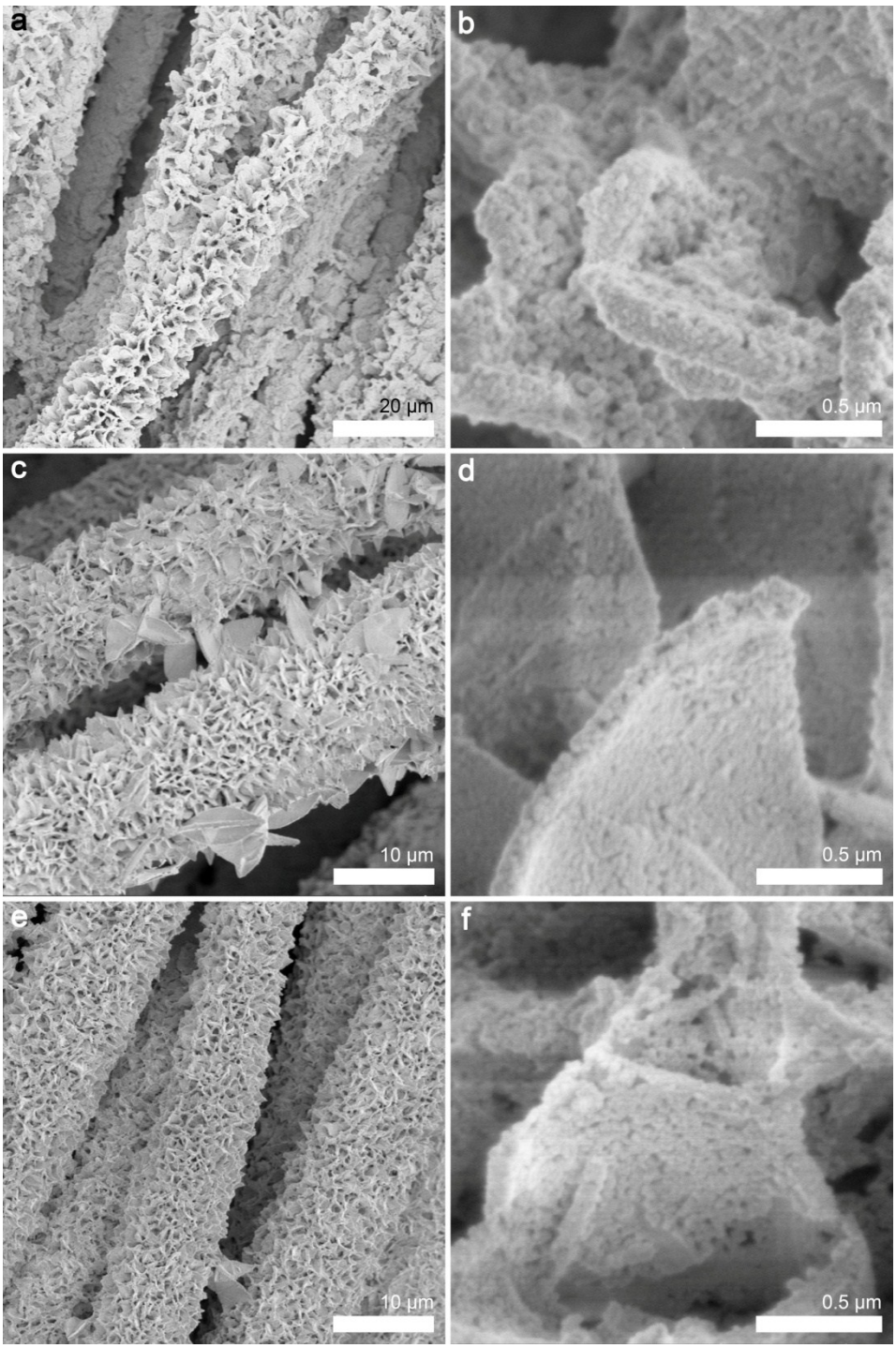

Fig. S13 (a) SEM images (at lower and higher magnification) of the products prepared with different quantity of NaClO. Effective Cl in NaClO: (a,b) 2 wt.%, (c,d) 6 wt.% and (e,f) 8 wt.%.

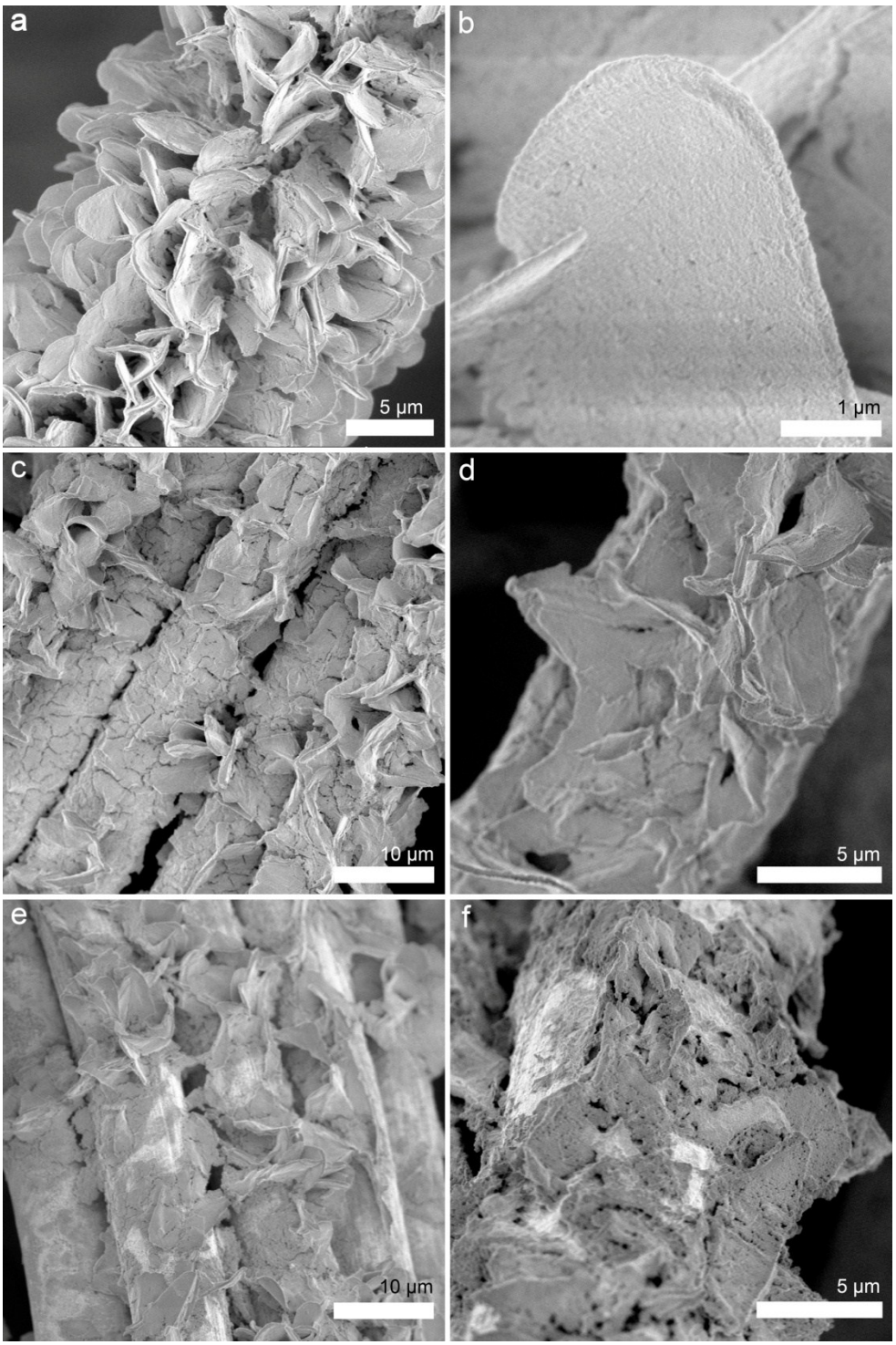

Fig. S14 SEM images of products prepared with 4 wt.% NaClO and different reaction time. (a,b) 5 min, (c,d) 30 min, and (e,f) 60 min.

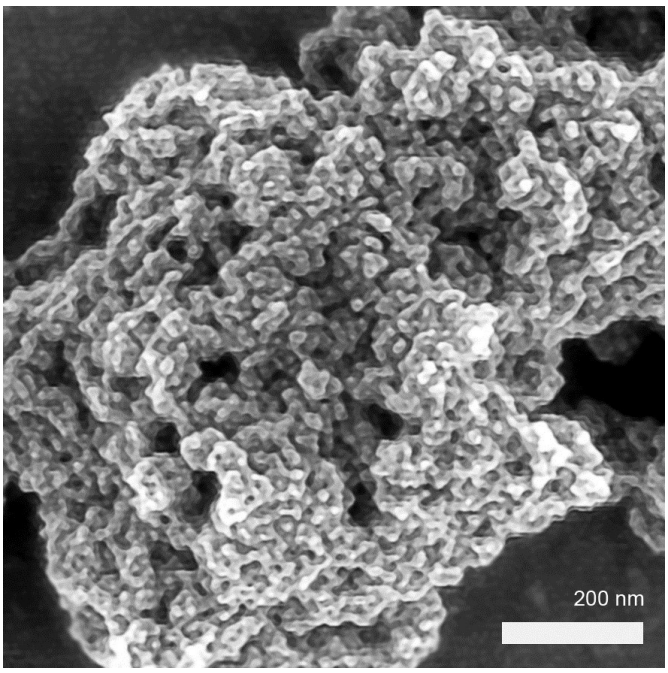

Fig. S15 SEM image of commercial RuO_2 nanoparticles.

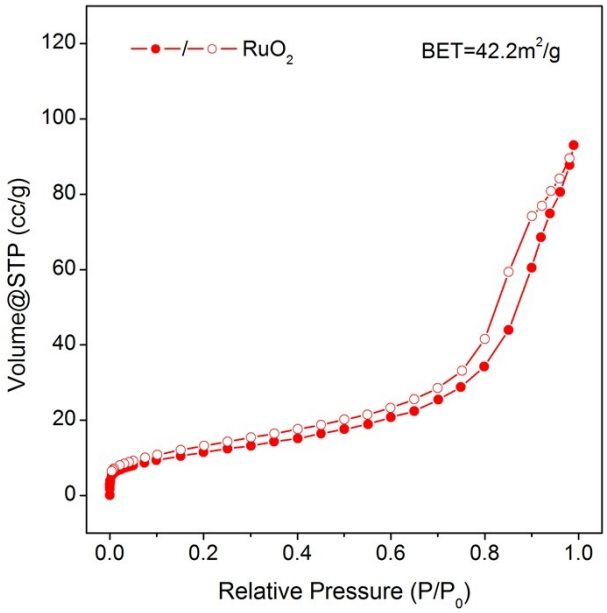

Fig. S16 N_2 sorption isotherms of commercial RuO_2 nanoparticles at 77 K.

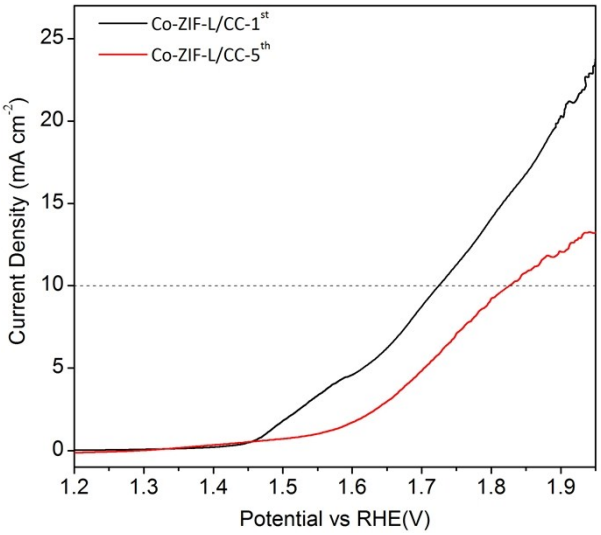

Fig. S17 Polarization curves of Co-ZIF-L/CC. The electrolyte was O_2-saturated 0.1 M PBS (pH = 7.0).

Due to the intrinsic instability of Co-ZIF-L, the electrocatalytic activity of Co-ZIF-L/CC electrode for neutral condition OER deteriorates rapidly during the OER process, indicated by the pronounced increase in the overpotential at a current density of 10 mA cm^{-2} from the initial value of 496 (the first scan) to 596 mV after 5 scans (Fig. S17). Meanwhile, the color of Co-ZIF-L/CC changes from bright purple to dark brown (Fig. S18). SEM images further show that the well-defined hierarchically porous nanostructure of Co-ZIF-L NSAs completely collapses within such a short time and transforms into layered nanostructures around each CC fiber (Fig. S19), which probably be assigned to cobalt oxides based on the unambiguous peaks in their PXRD pattern (Fig. S20).

Fig. S18 Optical images of Co-ZIF-L/CC before and after five LSV scans in 0.1 M PBS.

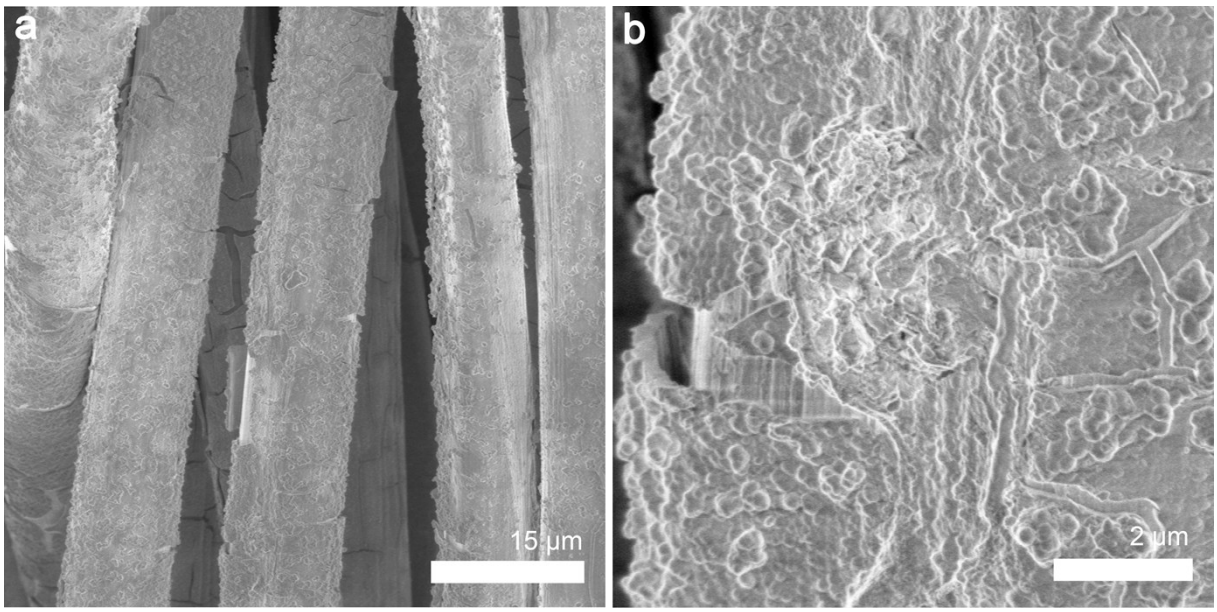

Fig. S19 SEM images of Co-ZIF-L/CC after five LSV scans in 0.1 M PBS.

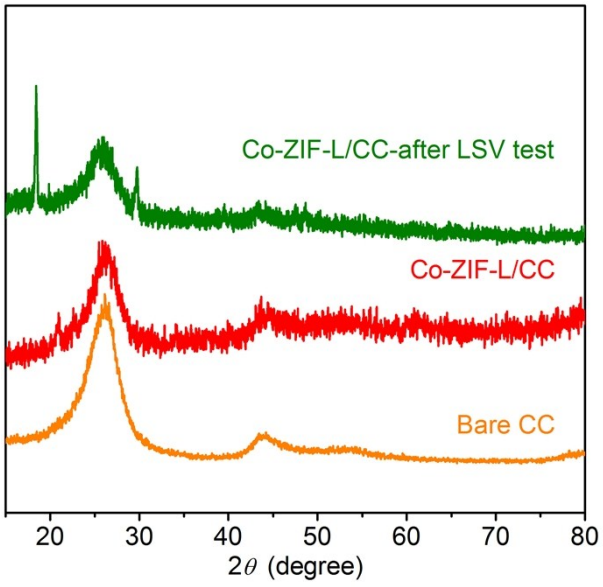

Fig. S20 PXRD patterns of Co-ZIF-L/CC before and after five LSV scans in 0.1 M PBS.

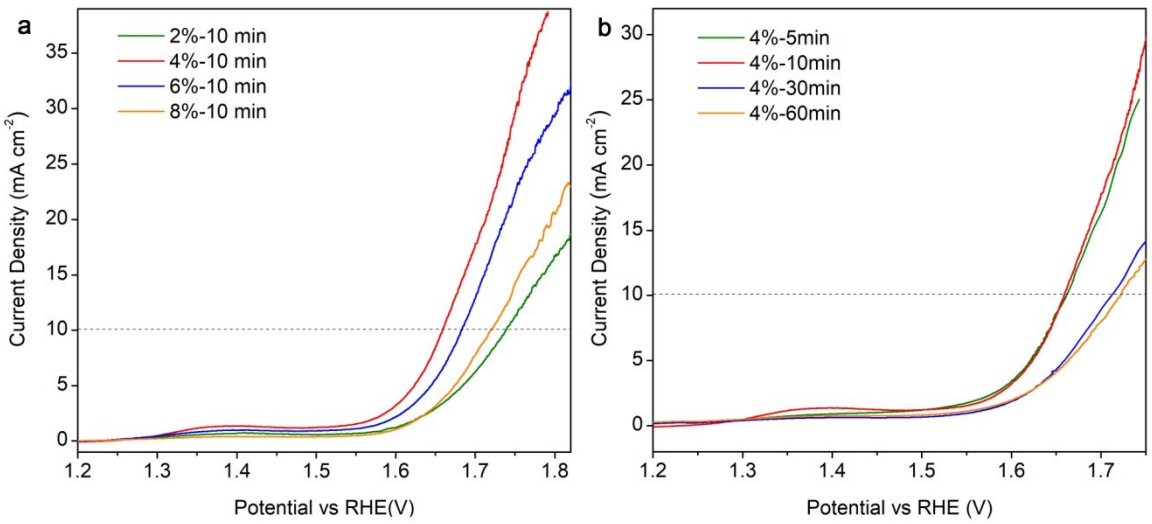

Fig. S21 Polarization curves of the products prepared with (a) different amount of NaClO or (b) different reaction time. The electrolyte was O_2-saturated 0.1 M PBS (pH = 7.0).

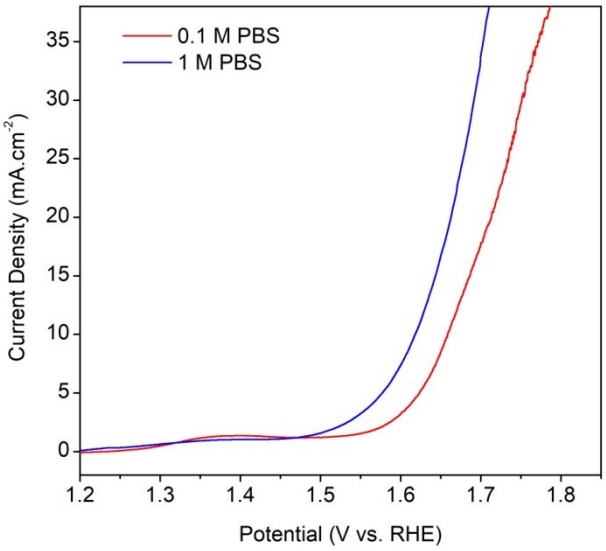

Fig. S22 Polarization curves of CoO_xH_y/CC electrode in PBS electrolyte of different concentration.

In principle, decrease in both the overpotential and Tafel slope should be expected upon the increase in PBS concentration from 0.1 to 1.0 M. However, our experimental results in fact show a decreased overpotential and an increased Tafel slope. The unexpected increase in the Tafel slope is likely due to the inevitable formation and deposition of cobalt(II, III) phosphate on the CoO_xH_y/CC surface, through the reaction between Co(II, III) ions and phosphate in the concentrated PBS solution (1 M potassium phosphate),[S14] and the cobalt(II, III) phosphate-induced structural deterioration of CoO_xH_y/CC (Fig. S24). The inevitable formation and deposition of cobalt(II, III) phosphate and the structural deterioration of CoO_xH_y/CC disfavors the kinetics of the OER reaction, and in turn leads to the deterioration in both the overpotential and Tafel slope during the first few LSV scans (Fig. S23). We emphasize here that even with such activity deterioration, the CoO_xH_y/CC is still capable of delivering exceptional performances (overpotential of 390 mV at 10 mA cm^{-2}, and Tafel slope of 141 mV dec^{-1}; cf. Fig. S22 and Table S4). Moreover, due to the typically X-Ray amorphous nature of the cobalt(II, III) phosphate formed in PBS solution,[S14] the exact identification of cobalt (II, III) phosphate is challenging, we thus provide two indirect

evidences, that is, the smoothed morphology due to the formation and deposition of cobalt(II, III) phosphate (Fig. S24a) and the appearance of P element in CoO_xH_y/CC after LSV test (Fig. S24b).

Moreover, as shown in Fig. S23, the polarization curve of the first scan in fact shows a pronounced Co^{3+}/Co^{4+} redox peak at *ca*. 1.4 V, which, however, rapidly declines and tends to stabilize after the fifth scan. The rapidly declined Co^{3+}/Co^{4+} redox peak at *ca*. 1.4 V – similar to the increase in the Tafel slope – is also probably due to the inevitable formation and deposition of cobalt(II, III) phosphate on the CoO_xH_y/CC surface in 1 M PBS and the cobalt(II, III) phosphate-induced structural deterioration of CoO_xH_y/CC, which impedes the efficient Co^{3+}/Co^{4+} redox transition and thus results in substantial activity loss during the initial stage (the first five scans).

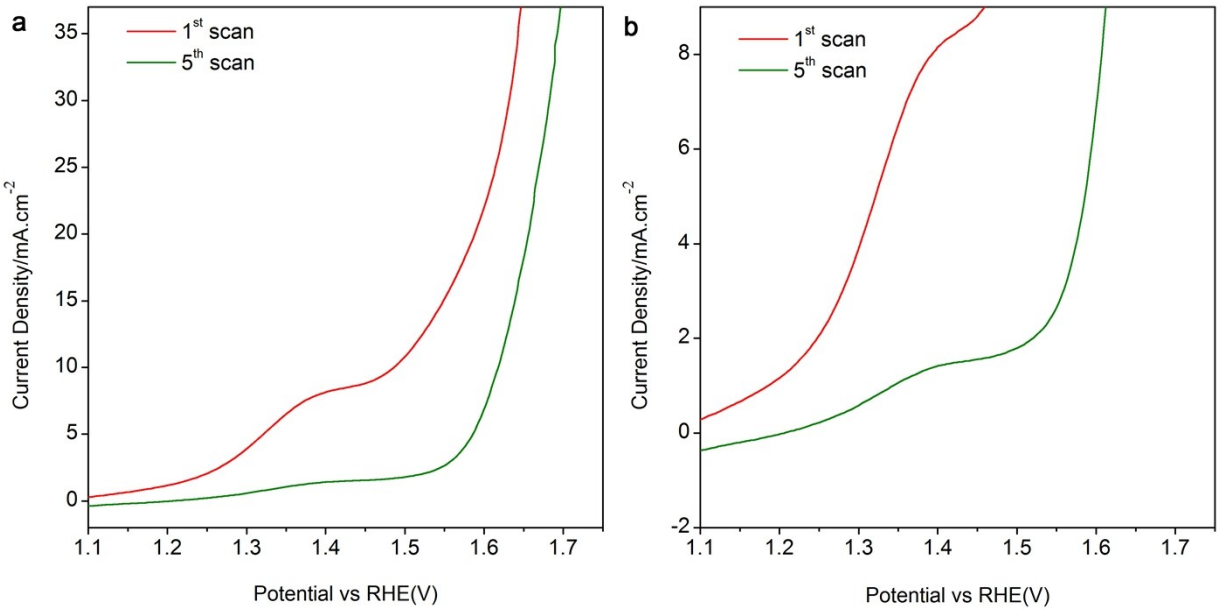

Fig. S23 Polarization curves of CoO_xH_y/CC electrode in 1.0 M PBS electrolyte. (a) Full curves, and (b) partially enlarged curves.

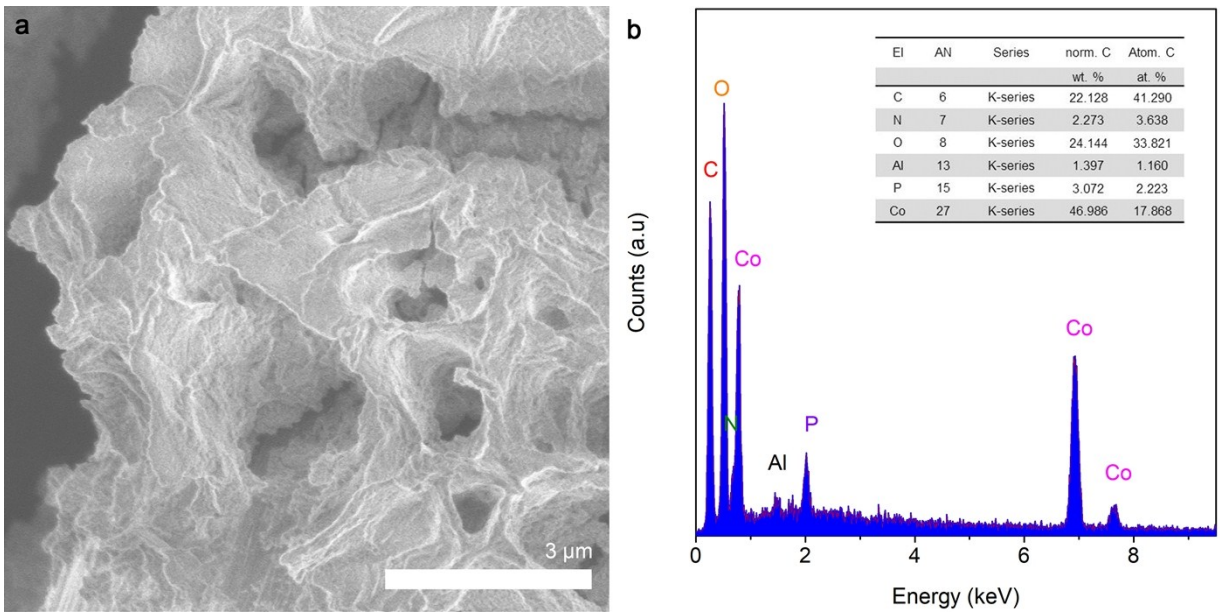

Fig. S24 (a) SEM image and (b) EDS spectrum of CoO_xH_y/CC after 5 LSV scans. Prior to characterization, the CoO_xH_y/CC was taken out the electrolyte after 5 LSV scans and carefully rinsed with copious ultrapure water.

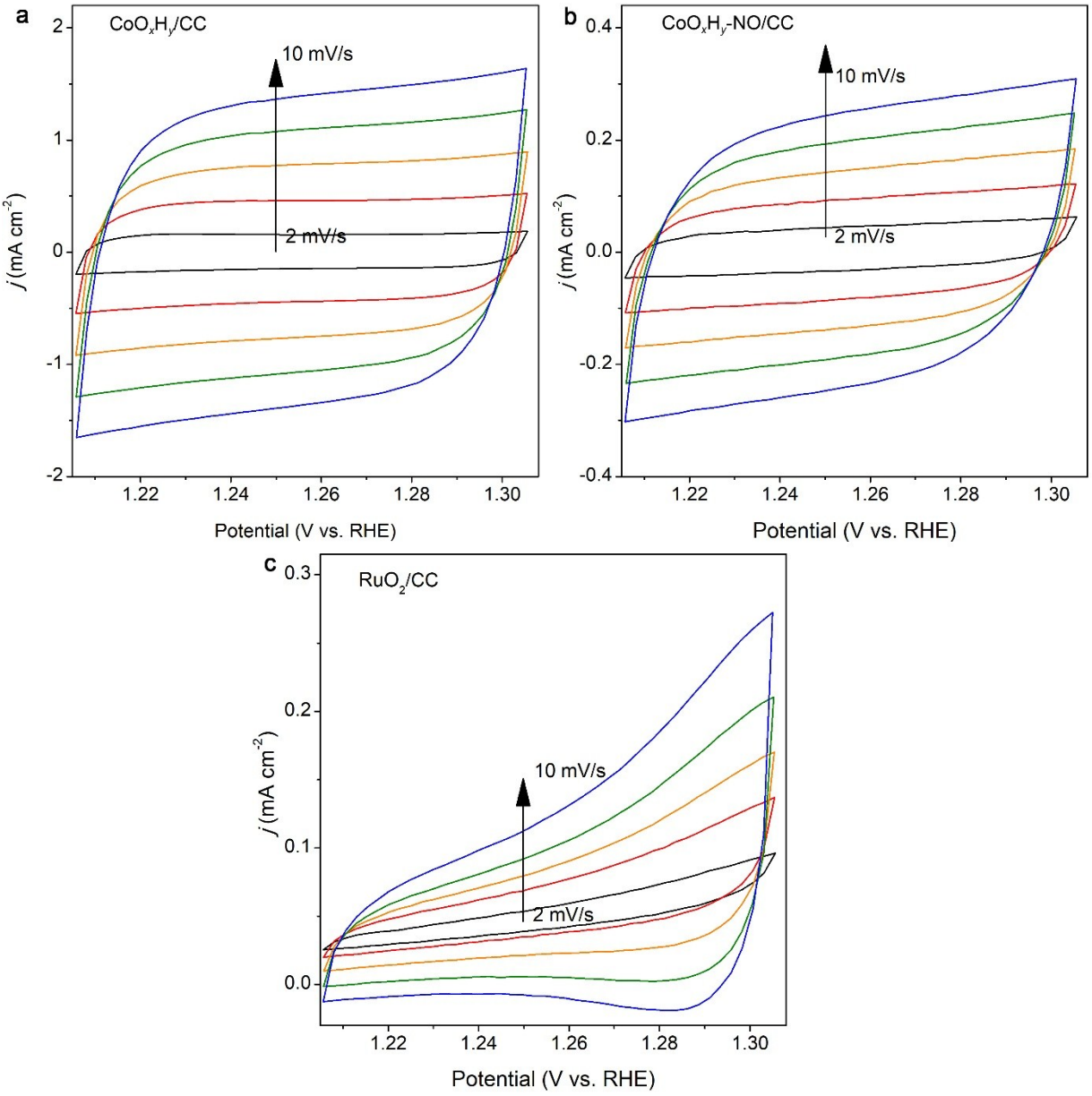

Fig. S25 CVs of (a) CoO_xH_y/CC, (b) CoO_xH_y-NO/CC, and (c) RuO_2/CC electrodes measured at scan rate ranging from 2 to 10 mV s^{-1}.

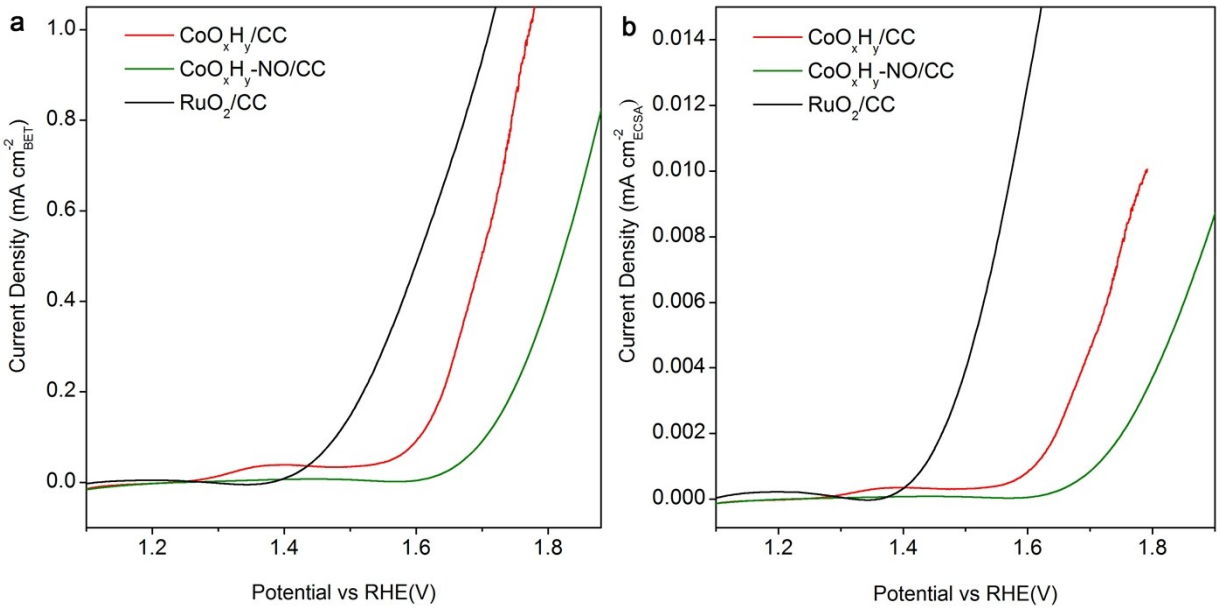

Fig. S26 Specific OER activity of CoO_xH_y/CC, CoO_xH_y-NO/CC and RuO_2/CC calculated by normalizing the current density in Fig. 4a against their corresponding (a) BET surface area and (b) ECSA. The ECSA is calculated by ECSA = C_{dl}/C_s, in which C_s, with a typical value of 40 μF cm^{-2}, is the specific capacitance of a flat, smooth surface of the electrode materials.[S2, 3]

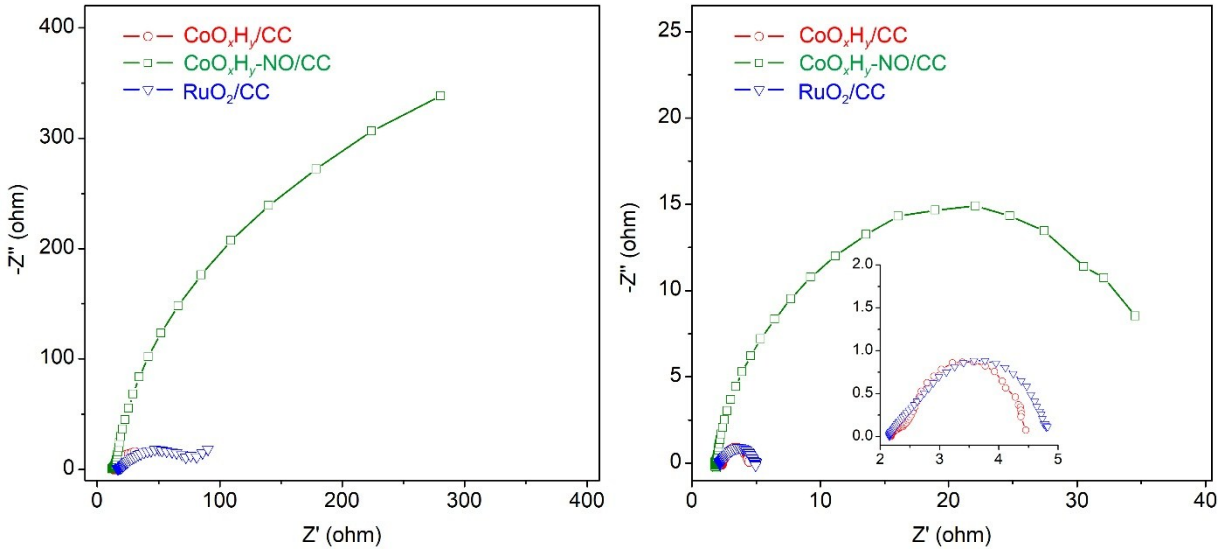

Fig. S27 EIS of the CoO_xH_y/CC, CoO_xH_y-NO/CC, and RuO_2/CC electrodes recorded in (a) 0.1 M PBS at 1.61 V vs RHE and (b) 1 M KOH solution at 1.55 V vs RHE.

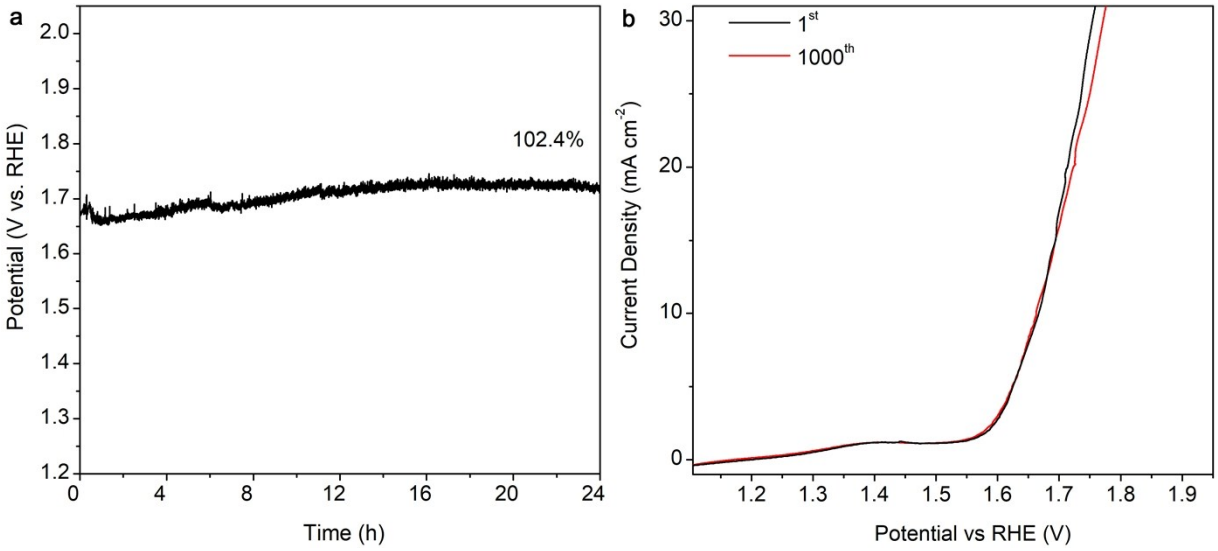

Fig. S28 (a) Chronopotentiometric curve of CoO_xH_y/CC at a constant current density of 10 mA cm^{-2} and (b) polarization curves before and after 1000 cycles in 0.1 M PBS.

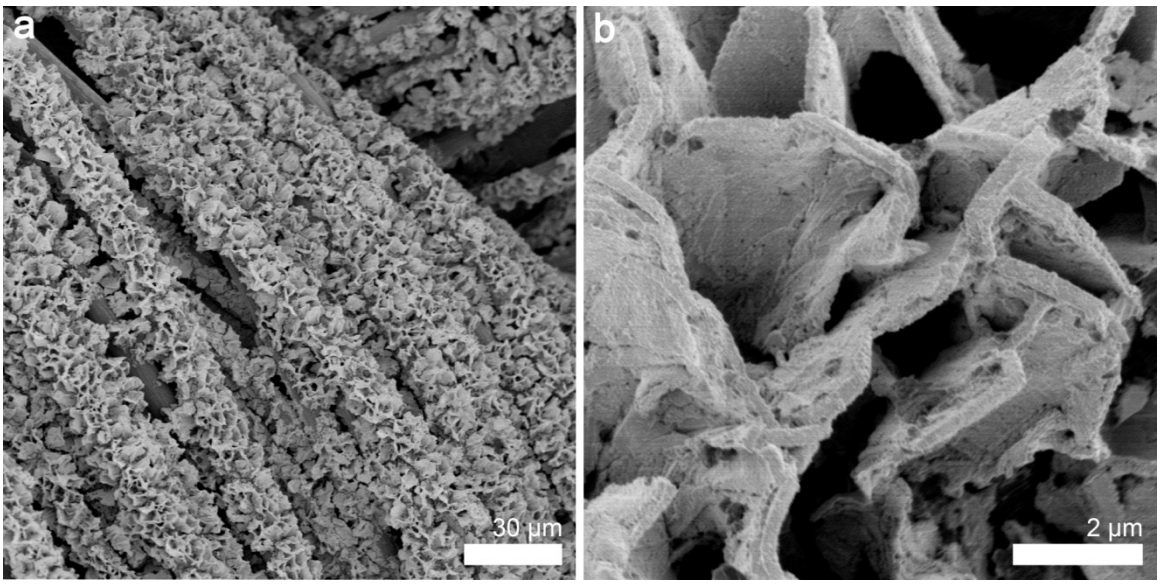

Fig. S29 SEM images of CoO_xH_y/CC electrode after the constant current test for 24 h in 0.1 M PBS.

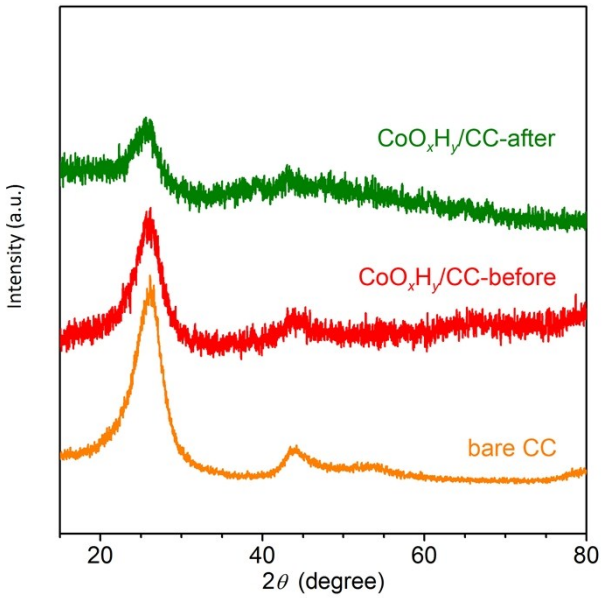

Fig. S30 PXRD patterns of CoO_xH_y/CC electrode before and after the constant current test for 24 h in 0.1 M PBS.

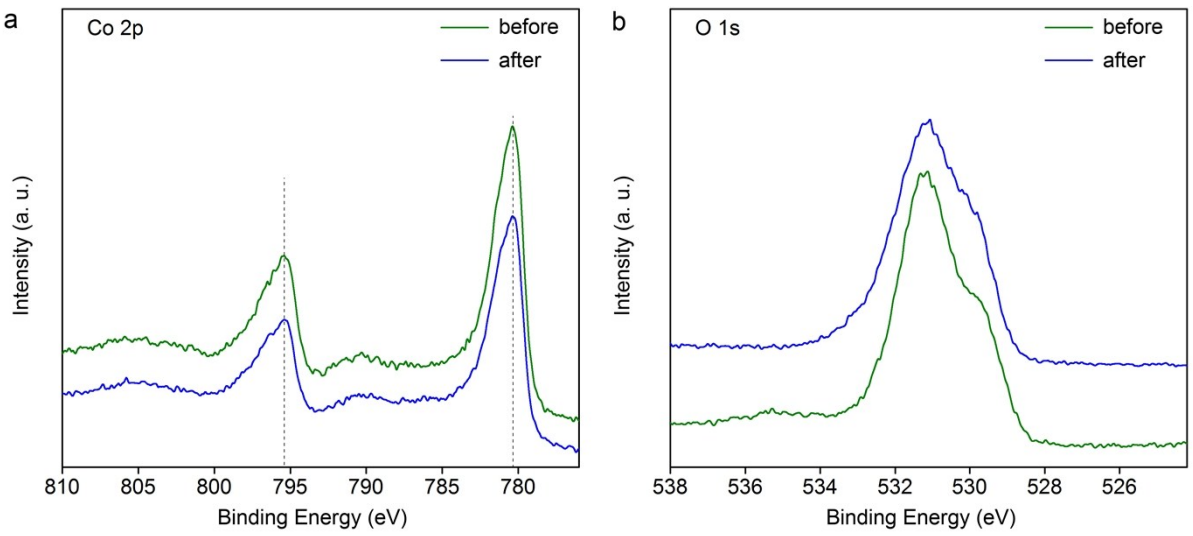

Fig. S31 XPS spectra of CoO_xH_y/CC electrode before and after the constant current test for 24 h in 0.1 M PBS.

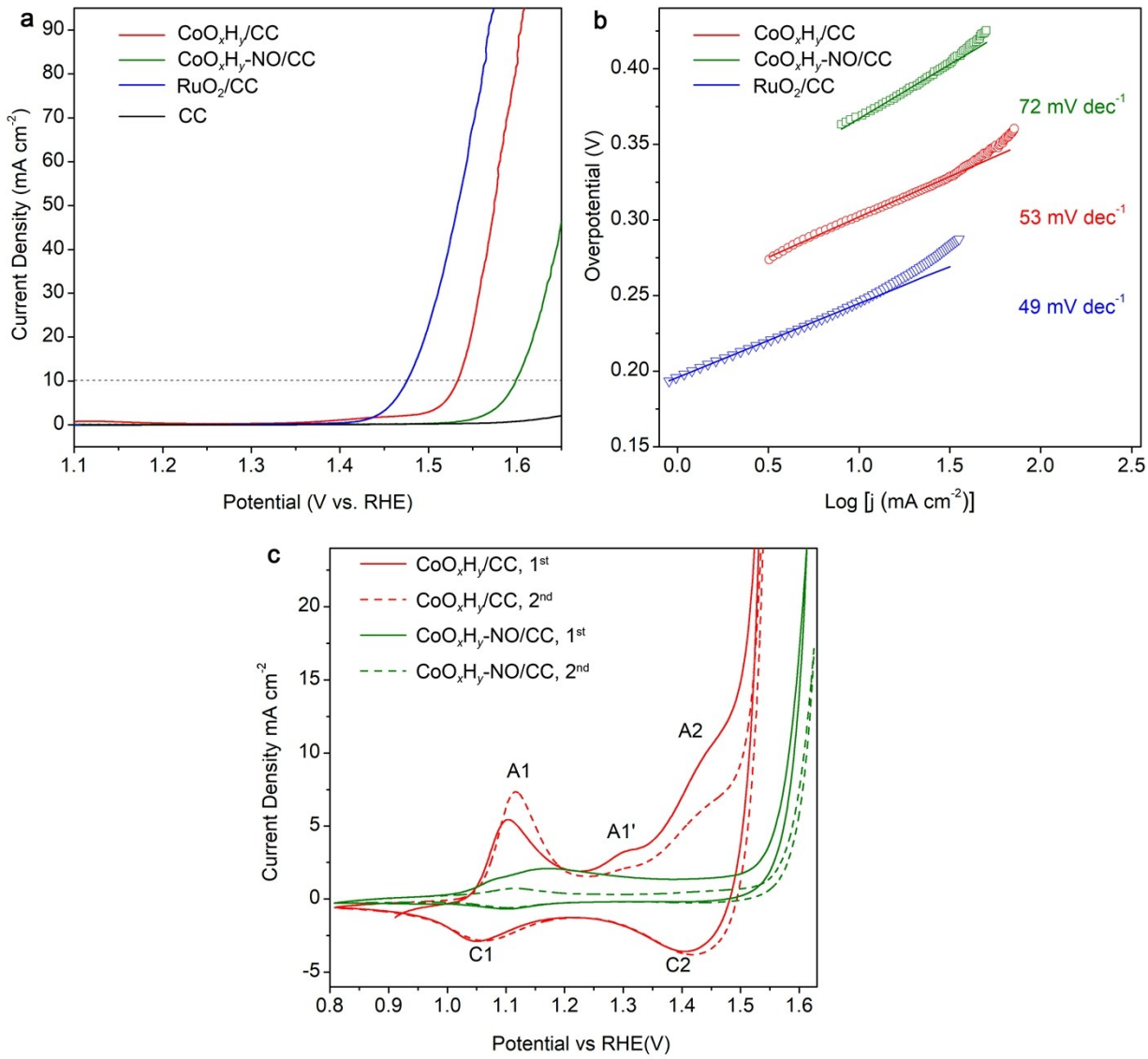

Fig. S32 (a) Polarization curves and (b) the corresponding Tafel plots for bare CC, RuO_2/CC, CoO_xH_y/CC and CoO_xH_y-NO/CC in 1 M KOH solution (pH = 13.7). (c) CVs of CoO_xH_y/CC and CoO_xH_y-NO/CC in 1 M KOH.

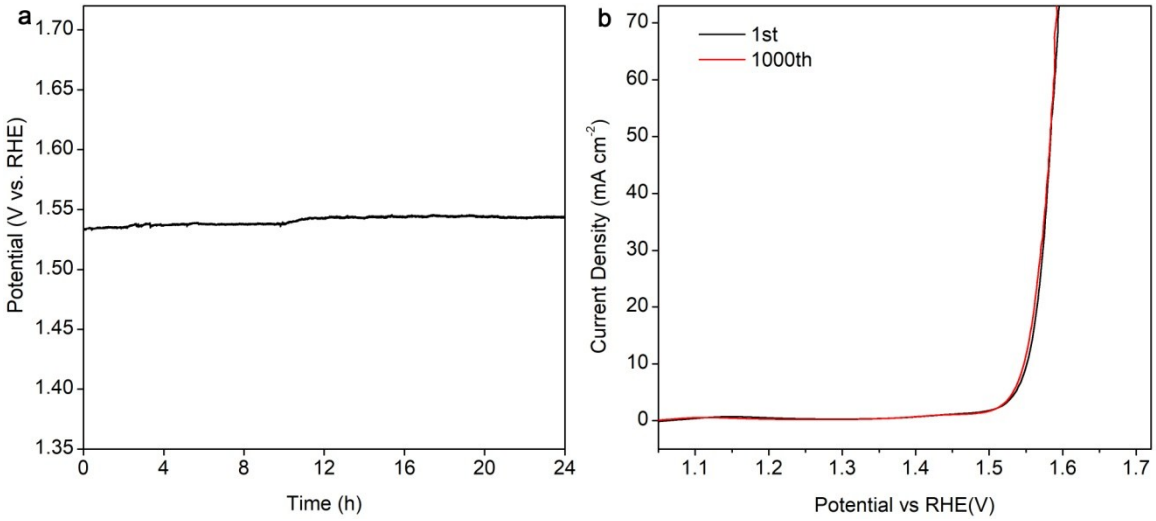

Fig. S33 (a) Chronopotentiometric curve of CoO_xH_y/CC electrode for 24 h at a constant current density of 10 mA cm^{-2} in 1M KOH solution. (b) LSV curves of the CoO_xH_y/CC electrode before and after 24 h's test in 1 M KOH solution.

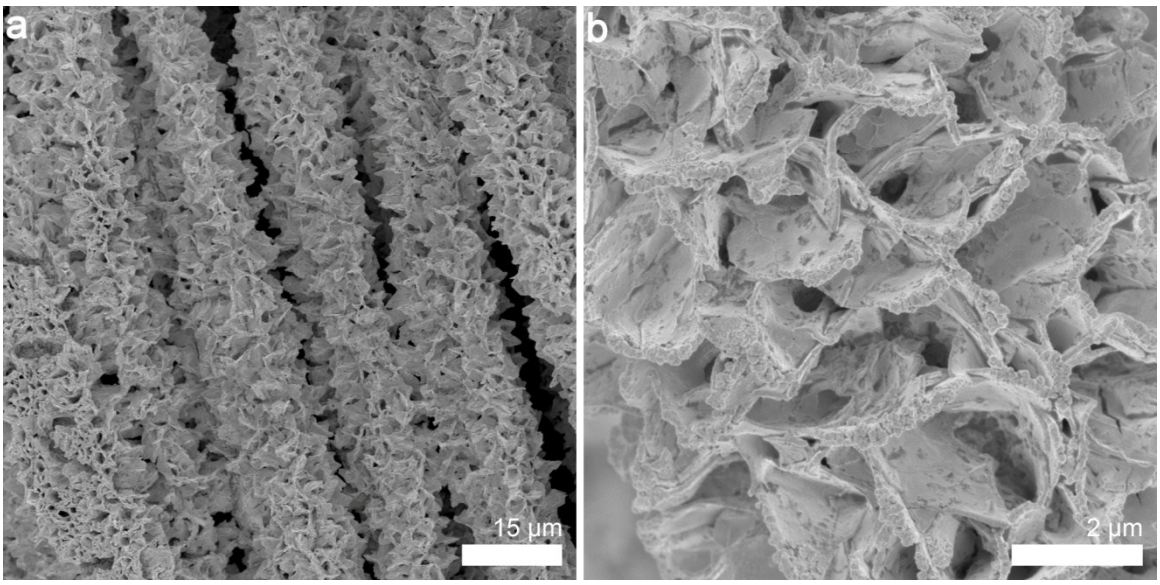

Fig. S34 SEM images at (a) low and (b) high magnification of CoO_xH_y/CC electrode after constant current test (10 mA cm^{-2}) for 24 h in 1 M KOH solution.

Table S4 Comparison of the OER activity under neutral condition between CoO_xH_y/CC and the high-performance cobalt-based catalysts reported recently in literature.

Catalyst	Substrate	Mass Loading (mg cm^{-2})	BET SA [h] (m^2 g^{-1})	ECSA [i] (cm^2)	Electrolyte	η_{onset} (mV)	η_{10} (mV)	*j* at 1.8 V	Tafel Slope (mV dec^{-1})	Reference
CoO_xH_y /CC	**CC [a]**	**0.8**	**438**	**3850**	**0.1 M PBS**		**430**	**38 [k]** **48 [l]/0.01 [m]**	**121**	**This work**
					1 M PBS		**390**		**141**	
MAF-X27-OH (Co)	GCE [b] 1200 rpm	0.2	1514	11.8	0.1M PBS	318		4.5 [k] 23 [l]/0.38 [m]	127	*J. Am. Chem. Soc.* 2016 [S15]
MAF-69-Mo	GCE	0.2	N/A [j]	N/A	0.1M PBS		490	22.0 [k]	144	*Angew. Chem. Int. Ed.* 2018 [S16]
A-CoO_xS_y	GCE	0.8	N/A	2225	0.1M PBS	270		4.59 [k] 5.7 [l]/0.002 [m]	164	*Angew. Chem. Int. Ed.* 2017 [S17]
Co-ZIF-9	FTO glass	0.3	N/A	N/A	pH = 7	370		0.6 [k] (1.92 V)	193	*Nanoscale* 2014 [S18]
Co-Bi NS/G [c]	GCE	0.285	N/A	NA	0.1 M PBS	235		14.4 [k]		*Angew. Chem. Int. Ed.* 2016 [S19]
Co-Bi NS [d]	GCE	0.285	N/A	NA	0.1 M PBS	366		5.3 [k]		
CoPi NA/Ti [e]	Ti mesh	0.95	N/A	33.9	0.1 M PBS		450		187	*Angew. Chem. Int. Ed.* 2017 [S20]
Ir-$Co(OH)_2$ [f]	GCE	0.566	N/A	20.6	1 M PBS		373		117.5	*Adv. Mater.* 2018 [S21]
$Co_{0.7}Fe_{0.3}P$/C NT	Carbon fiber paper	0.5	N/A	282.5	1 M PBS		500			*Adv. Funct. Mater.* 2017 [S2]
Co-Se-S@$Co(OH)_2$	CC [e]	2.0	N/A	25	0.1 M PBS		480			*ACS Appl. Mater. Interfaces* 2018 [S22]
Cu_6Co_7 Polyoxometalates	CC	1.0	N/A	N/A	0.2 M PBS		500		147	*J. Mater. Chem. A* 2018 [S23]
$NiCo_2S_4$ NS	CC	1.0	N/A	211.5	1 M PBS		402		123	*ACS Omega* 2018 [S24]
CoP NSA [g]	CC	2.6	N/A	1390	1 M PBS		536		257	*ChemElectroChem* 2017 [S25]

Annotations:

[a] CC, carbon cloth; [b] GCE, glassy carbon electrode; [c] G, graphene; [d] NS, nanosheet; [e] NA, nanoarray; [f] Ir-$Co(OH)_2$, atomic iridium (noble metal) incorporated (9.7 wt.%) in cobalt hydroxide; [g] NSA: nanosheet arrays; [h] SA: surface area; [i] ECSA: electrochemical active surface area; [j] N/A: not available; [k]: current density at 1.8 V normalized by geometric area, in the unit of mA cm^{-2}; [l]: current density at 1.8 V normalized by mass loading, in the unit of mA mg^{-1}; [m]: current density at 1.8 V normalized by ESCA, in the unit of mA.

Table S5. Comparison of the OER activities under alkaline conditions between CoO_xH_y/CC and the cobalt-based catalysts reported recently in literature.

Catalyst	Substrate	Electrolyte	η_{onset} (mV)	*j* at 1.8 V (mA cm^{-2})	Tafel Slope (mV dec^{-1})	Reference
CoO_xH_y /CC	**CC**	**1 M KOH**		**302**	**53**	**This work**
MAF-X27-OH (Co)	GCE 1200 rpm	1 M KOH		387	60	*J. Am. Chem. Soc.* 2016 [S15]
	Cu Foil (1mg cm^{-2})	1.0 M KOH		292	88	
A-CoO_xS_y	GCE	1 M KOH		290	67	*Angew. Chem. Int. Ed.* 2017 [S17]
A-CoO_x	GCE	1 M KOH		390	59	*ACS Catal.* 2018 [S26]
CoO_x@CN [a]	GCE	1 M KOH		260		*J. Am. Chem. Soc.* 2015 [S27]
CoO/N-doped graphene	GCE	1 M KOH	300	340	71	*Energy Environ. Sci.* 2014 [S28]
Co-Bi NS/G	GCE	1 M KOH		290	53	*Angew. Chem. Int. Ed.* 2016 [S19]

Annotations:

[a] CN, carbon nanotube.

Supplementary References

S1. J. Luo, J. H. Im, M. T. Mayer, M. Schreier, M. K. Nazeeruddin, N. G. Park, S. D. Tilley, H. J. Fan and M. Gratzel, *Science*, 2014, **345**, 1593-1596.

S2. X. Zhang, X. Zhang, H. Xu, Z. Wu, H. Wang and Y. Liang, *Adv. Funct. Mater.*, 2017, **27**, 1606635.

S3. C. Zhang, Y. Shi, Y. Yu, Y. Du and B. Zhang, *ACS Catal.*, 2018, **8**, 8077-8083.

S4. J. Yang, H. Liu, W. N. Martens and R. L. Frost, *J. Phys. Chem.*, 2010, **114**, 111-119.

S5. V. Pralong, A. Delahaye-Vidal, B. Beaudoin, B. Gérand and J. M. Tarascon, *J. Mater. Chem.*, 1999, **9**, 955-960.

S6. J. Huang, J. Chen, T. Yao, J. He, S. Jiang, Z. Sun, Q. Liu, W. Cheng, F. Hu, Y. Jiang, Z. Pan and S. Wei, *Angew. Chem. Int. Ed.*, 2015, **54**, 8722-8727.

S7. Q. Qi, Y. Chen, L. Wang, D. Zeng and D.-L. Peng, *Nanotechnology*, 2016, **27**, 455602.

S8. K. Deori and S. Deka, *CrystEngComm*, 2013, **15**, 8465-8474.

S9. W. Zhang, M. Han, Z. Jiang, Y. Song, Z. Xie, Z. Xu and L. Zheng, *ChemPhysChem*, 2007, **8**, 2091-2095.

S10. Y. Zhang, J. Zhu, X. Song and X. Zhong, *J. Phys. Chem.*, 2008, **112**, 5322-5327.

S11. X. Feng, W. Xing, L. Song and Y. Hu, *J. Mater. Chem. A*, 2014, **2**, 13299-13308.

S12. W. Fu, L. Long, M. Wang, Y. Yao, N. Wei, M. Yan, G. Yin, X. Liao, Z. Huang and X. Chen, *J. Alloys Compd.*, 2015, **631**, 82-85.

S13. C. Burlet, Y. Vanbrabant, H. Goethals, T. Thys and L. Dupin, *Spectrochim. Acta. A. Mol. Biomol. Spectrosc.*, 2011, **80**, 138-147.

S14. J. Wang and H. C. Zeng, *ACS Appl. Mater. Interfaces*, 2018, **10**, 6288-6298.

S15. X.-F. Lu, P.-Q. Liao, J.-W. Wang, J.-X. Wu, X.-W. Chen, C.-T. He, J.-P. Zhang, G.-R. Li and X.-M. Chen, *J. Am. Chem. Soc.*, 2016, **138**, 8336-8339.

S16. Y.-T. Xu, Z.-M. Ye, J.-W. Ye, L.-M. Cao, R.-K. Huang, J.-X. Wu, D.-D. Zhou, X.-F. Zhang, C.-T. He, J.-P. Zhang and X.-M. Chen, *Angew. Chem. Int. Ed.*, 2019, **58**, 139-143.

S17. P. Cai, J. Huang, J. Chen and Z. Wen, *Angew. Chem. Int. Ed.*, 2017, **56**, 4858-4861.

S18. S. Wang, Y. Hou, S. Lin and X. Wang, *Nanoscale*, 2014, **6**, 9930-9934.

S19. P. Chen, K. Xu, T. Zhou, Y. Tong, J. Wu, H. Cheng, X. Lu, H. Ding, C. Wu and Y. Xie, *Angew. Chem. Int. Ed.*, 2016, **55**, 2488-2492.

S20. L. Xie, R. Zhang, L. Cui, D. Liu, S. Hao, Y. Ma, G. Du, A. M. Asiri and X. Sun, *Angew. Chem. Int. Ed.*, 2017, **56**, 1064-1068.

S21. Y. Zhang, C. Wu, H. Jiang, Y. Lin, H. Liu, Q. He, S. Chen, T. Duan and L. Song, *Adv. Mater.*, 2018, **30**, 1707522.

S22. Z.-M. Luo, J.-W. Wang, J.-B. Tan, Z.-M. Zhang and T.-B. Lu, *ACS Appl. Mater. Interfaces*, 2018, **10**, 8231-8237.

S23. M. Wang, W. Zhong, S. Zhang, R. Liu, J. Xing and G. Zhang, *J. Mater. Chem. A*, 2018, **6**, 9915-9921.

S24. S. Hyun and S. Shanmugam, *ACS Omega*, 2018, **3**, 8621-8630.

S25. T. Liu, L. Xie, J. Yang, R. Kong, G. Du, A. M. Asiri, X. Sun and L. Chen, *ChemElectroChem*, 2017, **4**, 1840-1845.

S26. L. Liardet and X. Hu, *ACS Catal.*, 2018, **8**, 644-650.

S27. H. Jin, J. Wang, D. Su, Z. Wei, Z. Pang and Y. Wang, *J. Am. Chem. Soc.*, 2015, **137**, 2688-2694.

S28. S. Mao, Z. Wen, T. Huang, Y. Hou and J. Chen, *Energy Environ. Sci.*, 2014, **7**, 609-616.